



# ALMA High-frequency Long Baseline Campaign in 2021: Highest Angular Resolution Submillimeter Wave Images for the Carbon-rich Star R Lep

Yoshiharu Asaki<sup>1,2,3</sup> , Luke T. Maud<sup>4,5</sup> , Harold Francke<sup>1</sup> , Hiroshi Nagai<sup>6</sup> , Dirk Petry<sup>4</sup> , Edward B. Fomalont<sup>7</sup> , Elizabeth Humphreys<sup>1,8</sup> , Anita M. S. Richards<sup>9</sup> , Ka Tat Wong<sup>10,11</sup> , William Dent<sup>1</sup> , Akihiko Hirota<sup>1,2</sup> ,

Jose Miguel Fernandez<sup>12</sup>, Satoko Takahashi<sup>6</sup> , and Antonio S. Hales<sup>1,7</sup>

<sup>1</sup> Joint ALMA Observatory, Alonso de Córdova 3107, Vitacura 763 0355, Santiago, Chile; [yoshiharu.asaki@nao.ac.jp](mailto:yoshiharu.asaki@nao.ac.jp)

<sup>2</sup> National Astronomical Observatory of Japan, Los Abedules 3085 Oficina 701, Vitacura 763 0414, Santiago, Chile

<sup>3</sup> Department of Astronomical Science, School of Physical Sciences, The Graduate University for Advanced Studies, SOKENDAI, 2-21-1 Osawa, Mitaka, Tokyo 181-8588, Japan

<sup>4</sup> ESO Headquarters, Karl-Schwarzschild-Str. 2, D-85748 Garching, Germany

<sup>5</sup> Allegro, Leiden Observatory, Leiden University, PO Box 9513, 2300 RA Leiden, The Netherlands

<sup>6</sup> National Astronomical Observatory of Japan, 2-21-1 Osawa, Mitaka, Tokyo 181-8588, Japan

<sup>7</sup> National Radio Astronomy Observatory, 520 Edgemont Road, Charlottesville, VA 22903, USA

<sup>8</sup> ESO Vitacura, Alonso de Cordova 3107, Santiago, Chile

<sup>9</sup> Jodrell Bank Centre for Astrophysics, Department of Physics and Astronomy, University of Manchester, M13 9PL, UK

<sup>10</sup> IRAM ARC node, Institut de Radioastronomie Millimétrique, 300 rue de la Piscine, F-38406 Saint-Martin-d'Hères, France

<sup>11</sup> Theoretical Astrophysics, Department of Physics and Astronomy, Uppsala University, Box 516, SE-751 20 Uppsala, Sweden

<sup>12</sup> Lowell Observatory, 1400 W Mars Hill Road, Flagstaff, AZ 86001, USA

Received 2023 April 10; revised 2023 August 30; accepted 2023 August 31; published 2023 November 15

## Abstract

The Atacama Large Millimeter/submillimeter Array (ALMA) was used in 2021 to image the carbon-rich evolved star R Lep in Bands 8–10 (397–908 GHz) with baselines up to 16 km. The goal was to validate the calibration, using band-to-band (B2B) phase referencing with a close phase calibrator J0504-1512, 1°2 from R Lep in this case, and the imaging procedures required to obtain the maximum angular resolution achievable with ALMA. Images of the continuum emission and the hydrogen cyanide (HCN) maser line at 890.8 GHz, from the  $J = 10-9$  transition between the (11<sup>1</sup>0) and (04<sup>0</sup>0) vibrationally excited states, achieved angular resolutions of 13, 6, and 5 mas in Bands 8–10, respectively. Self-calibration (self-cal) was used to produce ideal images to compare with the B2B phase referencing technique. The continuum emission was resolved in Bands 9 and 10, leaving too little flux for the self-cal of the longest baselines, so these comparisons are made at coarser resolution. Comparisons showed that B2B phase referencing provided phase corrections sufficient to recover 92%, 83%, and 77% of the ideal image continuum flux densities. The HCN maser was sufficiently compact to obtain self-cal solutions in Band 10 for all baselines (up to 16 km). In Band 10, B2B phase referencing as compared to the ideal images recovered 61% and 70% of the flux density for the HCN maser and continuum, respectively.

*Unified Astronomy Thesaurus concepts:* [Long baseline interferometry \(932\)](#); [Submillimeter astronomy \(1647\)](#); [Phase error \(1220\)](#)

## 1. Introduction

### 1.1. ALMA Evolution to High Angular Resolution

The Atacama Large Millimeter/submillimeter Array (ALMA), located on the Chajnantor plain of the Atacama desert in Chile, is a large and sensitive radio array designed to image celestial sources at millimeter to submillimeter wavelengths. A detailed description of the observatory at the time of the observations discussed here can be found in Cortes et al. (2022). The telescope system consists of two arrays and one single dish cluster. One of the arrays, designated as the 12 m array, contains up to fifty 12 m diameter antennas, and provides a range of angular resolutions by reconfiguring the antenna locations within 10 different configurations. The approximate angular resolution of a radio array is roughly  $\lambda/B_{\max}$  rad, where  $\lambda$  is the observing wavelength, and  $B_{\max}$  is the longest baseline

length projected to the target source in the array.<sup>13</sup> The highest angular resolution possible with the 12 m array is achieved in Configuration 10, with the longest baseline length of 16.2 km.

Relatively compact configurations were available in early ALMA observing cycles, while progressively longer baselines or higher frequencies have been made available during the period of 2013–2019 based on capabilities confirmation. In 2013, the first relatively long baselines of 2.7 km were coordinated by putting three remote antennas located far from the regular 12 m array to make science verification experiments at 350 GHz (Band 7) and 650 GHz (Band 9) (Richards et al. 2014). In 2014, the 12 m array was used for the first time in the most extended configuration with the longest baselines of 16 km using Bands 3 (84–116 GHz), 4 (125–163 GHz), 6 (211–275 GHz), and 7 (275–373 GHz)

Original content from this work may be used under the terms of the [Creative Commons Attribution 4.0 licence](#). Any further distribution of this work must maintain attribution to the author(s) and the title of the work, journal citation and DOI.

<sup>13</sup> In the case of a large array with an antenna distribution like that of ALMA, a more accurate estimate of angular resolution replaces  $B_{\max}$  with  $L_{80}$ , i.e., the baseline length corresponding to the 80th percentile of the baseline length distribution, see Cortes et al. (2022).

(ALMA Partnership et al. 2015a, 2015b, 2015c, 2015d; Matthews et al. 2015; Vlemmings et al. 2015; Wong et al. 2016).

On the other hand, ALMA’s longest baseline capability had not been opened to users of the highest frequency bands (Bands 8–10). Using a phase reference calibrator as close as possible to the target was found to be critical in relatively long baseline ( $>3.6$  km), high-frequency (HF) observations from the interferometric phase stability point of view. An approximate guideline is that the phase calibrator should be within  $4^\circ$  at Band 7 for the most extended configurations and less distant at Bands 8 (385–500 GHz), 9 (602–720 GHz) and 10 (787–950 GHz) (Maud et al. 2020, hereafter M20). However, the sky number density of suitable phase calibrators decreases at higher frequencies since the majority of phase calibrators are quasars, which become fainter at higher frequencies while the atmospheric attenuation for the submillimeter waves becomes larger (Asaki et al. 2020a, hereafter A20).

In order to overcome the difficulties in finding a close phase calibrator in the HF bands, ALMA needed to wait for the validation of the novel phase calibration technique using band-to-band (B2B) phase referencing (Asaki et al. 2016). With this calibration method, a phase calibrator is observed at a lower frequency, and then the phase corrections are derived by scaling the solutions up to the target frequency (e.g., Asaki et al. 1998; Dodson & Rioja 2009; Pérez et al. 2010). In using B2B phase referencing, the number of usable phase calibrators is increased and it becomes possible to find a calibrator closer to the science target (typically  $<3^\circ$ , Maud et al. 2023b) compared to the case where the calibrator is required to be at the same frequency as the science target.

The initial High-frequency Long Baseline Campaign in 2017 (HF-LBC-2017) was arranged to explore B2B phase referencing using the 12 m array with up to 16 km baselines in Bands 7–9 (Asaki et al. 2020a, 2020b; M20; Maud et al. 2022, hereafter M22). In parallel, verification of an antenna fast switching to alternate scans between the phase calibrator and target as quickly as possible during an observation was being tested to mitigate the fast visibility phase variations due to atmospheric phase fluctuations. The switching cycle time ( $t_{\text{swt}}$ ) is defined as a time interval between two successive phase calibrator scans: such that phase referencing corrects the timescale phase variations between the phase calibrator and the target scans longer than that with the timescale of  $t_{\text{swt}}/2$  (Carilli & Holdaway 1999). Thus, fast switching acts to minimize achievable and correct phases over short timescales. The experiments and tests of the ALMA fast switching in M22 suggest that  $t_{\text{swt}}$  should be no longer than 60 s for ALMA long baseline observations in Bands 8–10, with the proviso that the phase calibrator is also close to the target.

In the 2019 High-frequency Long Baseline Campaign (HF-LBC-2019), a combination of B2B phase referencing and fast switching was extensively tested in Bands 8–10, and the impact of the phase calibrator separation angle was investigated. In the tests, bright quasars were used as both the phase calibrator and target sources, and images with an angular resolution of the minor axis of the synthesized beam of  $\sim 5$  mas were achieved (Maud et al. 2023b). HF-LBC-2019 demonstrated that either standard phase calibration (in-band phase referencing) or B2B phase referencing produced *good image quality* (Section 2.2) when using a sufficiently close phase calibrator. For example, for Band 10 and 16 km baselines, a visibility phase residual rms of  $\leq 1$  rad

could be achieved by selecting a phase calibrator with a separation angle of  $\leq 1^\circ$  and provided that the atmospheric phase stability was  $\leq 30^\circ$  as measured over  $t_{\text{swt}}$  (Maud et al. 2023b).

Following the positive results of HF-LBC-2019, the High-Frequency Long Baseline Campaign in 2021 (HF-LBC-2021) was organized to observe a compact target with an extended array configuration, including 16 km baselines using the same observing and data processing procedures as in users’ observations. We selected R Lep, a carbon-rich, mass-losing asymptotic giant branch (AGB) star, of which the continuum emission was thought to be compact from low angular resolution ALMA observations in Bands 6 and 7 (Ramstedt et al. 2020), and Band 10 (Wong 2019). It has a sufficiently close phase calibrator ( $1.2^\circ$ ) when using B2B phase referencing, and the star has relatively strong continuum emission and a bright, narrow maser line in Band 10. R Lep was observed in three experiments, one in each of Bands 8–10.

The HF-LBC-2021 experiments with R Lep as the science target are described as follows: Section 2 provides an overview and the technical background of the experiments. Section 3 briefly details the data reduction and calibration procedure. Section 4 presents the observation results for the target source, while a discussion of these results follows in Section 5. Phase calibrators are likely to show resolved structure at high angular resolution, and Section 5 discusses the implications if a calibrator turns out to be resolved. Finally, we summarize the paper in Section 6.

### 1.2. The Carbon-rich Star R Lep

R Lep is a Mira-type variable with a period of 445 days (Watson et al. 2006) at a distance of  $471_{-64}^{+88}$  pc, based on the estimate by Andriantsaralaza et al. (2022) using the third Gaia data release (DR3; Vallenari et al. 2023). R Lep has an apparently spherical shape and a diameter of  $15.20 \pm 0.20$  mas at a pulsation phase of 0.20, in the near-infrared *K* band ( $2.0\text{--}2.4 \mu\text{m}$ ), as measured by the Very Large Telescope Interferometer (VLTI; Hofmann et al. 2005). We adopt a systemic velocity of  $11.5 \text{ km s}^{-1}$  and an outflow velocity of  $19 \text{ km s}^{-1}$  based on the CO observations of Ramstedt et al. (2020). The coordinates of the star are  $(04^{\text{h}}59^{\text{m}}36^{\text{s}}.35, -14^\circ 48' 22'')$  in the International Celestial Reference System (ICRS) at J2000. The continuum emission of AGB stars at radio and (sub)millimeter wavelengths is consistent with the *radio photosphere* model, in which the dominant opacity is caused by free–free interactions between electrons and neutral H and H<sub>2</sub>, and the spectral index is roughly 2 in the radio domain (Reid & Menten 1997; Planesas et al. 2016). The continuum flux densities of R Lep in Bands 6 (224 GHz) and 7 (338 GHz), as measured from the images provided by Ramstedt et al. (2020) at the CDS,<sup>14</sup> are 16 and 27 mJy, respectively, implying a spectral index of  $\sim 1.3$ . The flux density at Band 10 (890 GHz) is expected to be  $\gtrsim 100$  mJy.

Mass loss from AGB stars builds up a circumstellar envelope (CSE) rich in molecules and dust. In using different molecular species we can probe the CSE, and therefore the mass-loss process, at different radii from the central stars. Hydrogen cyanide (HCN) is one of the most abundant molecules in carbon-rich CSEs and is known to exhibit maser action in many

<sup>14</sup> Strasbourg Astronomical Data Center, <https://cdsarc.u-strasbg.fr/viz-bin/cat/J/A+A/640/A133>.

**Table 1**  
Experiments in HF-LBC-2021

| Exp Code | Epoch       | Time (UTC)<br>(hh:mm) | HF Band<br>( $\nu_{\text{HF}}$ GHz) <sup>a</sup> | LF Band<br>( $\nu_{\text{LF}}$ GHz) <sup>a</sup> | Number of<br>Antennas | Total ON-source<br>Duration for R Lep (s) | Execution Block<br>(uid://A002/) |
|----------|-------------|-----------------------|--|--|-----------------------|---|----------------------------------|
| (1)      | (2)         | (3)                   | (4)  | (5)  | (6)                   | (7)                                       | (8)                              |
| B-08     | 2021 Sep 23 | 07:30–09:17           | Band 8 (405)                                     | Band 4 (135)                                     | 44                    | 1580                                      | Xf0e992/X4d18                    |
| B-09     | 2021 Sep 10 | 09:28–11:33           | Band 9 (670)                                     | Band 4 (148)                                     | 42                    | 1643                                      | Xf07268/X32f0                    |
| B-10     | 2021 Sep 09 | 08:44–10:20           | Band 10 (896)                                    | Band 7 (299)                                     | 39                    | 1722                                      | Xf06573/X20d3                    |

**Note.**

<sup>a</sup> Local oscillator frequency of the SIS mixer in the receiver cold cartridge, corresponding to the center RF frequency in the receiving bandwidth.

**Table 2**  
Observed Calibrator Sources in the HF-LBC-2021 Experiments

| Exp Code | DGC Source | HF Flux Calibrator | HF Bandpass Calibrator | Check Source (Separation from Phase Calibrator) |
|----------|------------|--------------------|------------------------|---|
| (1)      | (2)        | (3)                | (4)                    | (5)   |
| B-08     | J0522-3627 | J0522-3627         | J0423-0120             | J0516-1603 (3 $^{\circ}$ 0)                     |
| B-09     | J0522-3627 | J0522-3627         | J0522-3627             | J0438-1251 (6 $^{\circ}$ 7)                     |
| B-10     | J0522-3627 | J0522-3627         | J0522-3627             | J0423-0120 (17 $^{\circ}$ 2)                    |

transitions in the (sub)millimeter domain (e.g., Guilloteau et al. 1987; Bieging 2001; Smith et al. 2014; Menten et al. 2018), especially in the vibrationally excited states of the bending mode (see Table A.1 of Jeste et al. 2022, for a list of known HCN maser from C-rich CSEs to date). There are two submillimeter HCN masers at 804.75 and 890.76 GHz, first detected in C-rich CSEs by Schilke et al. (2000) and Schilke & Menten (2003), respectively, using the Caltech Submillimeter Observatory (CSO) 10.4 m telescope on Maunakea, which are observable in Band 10 with ALMA. The HCN maser targeted in R Lep is that at 890.7607 GHz, from the  $J = 10-9$  transition between the ( $11^1_0$ ) and ( $04^0_0$ ) vibrationally excited states with an upper-level energy above 4260 K (Hocker & Javan 1967; Barber et al. 2014).

Circumstellar astronomical masers have only been resolved on milliarcsecond scales previously around O-rich stars. SiO masers occur within a few stellar radii, where we expect to find the HCN masers. SiO masers emanate from clumps with a typical extent of  $\sim 1$  au (Assaf 2018) while the individual, beamed spots are much smaller (as established by component fitting). At the distance of R Lep, 1 au corresponds to an angular size of 2.1 mas, which cannot be resolved directly even with ALMA’s highest angular resolution of 5 mas. A whole SiO maser shell would have a diameter  $\lesssim 50$  mas at the distance of R Lep (e.g., Cotton et al. 2004), just within the ALMA Band 10 maximum recoverable scale.

Wong (2019) reported the first ALMA imaging of bright HCN masers toward C-rich stars including R Lep at an angular resolution of  $\sim 0''.1$ , and found that the spatial structure of the HCN masers is generally not well resolved, confirming previous predictions that these masers should arise very close to the star (Schilke & Menten 2003). This gives us some a priori knowledge about the probable properties of target images in these long baseline experiments. The bright and relatively compact maser emission also makes it easy to perform self-calibration (self-cal), which is helpful in assessing the image coherence (see Section 3.5.2). Therefore, R Lep is an excellent target for use in fully validating ALMA’s long baseline capability in Band 10.

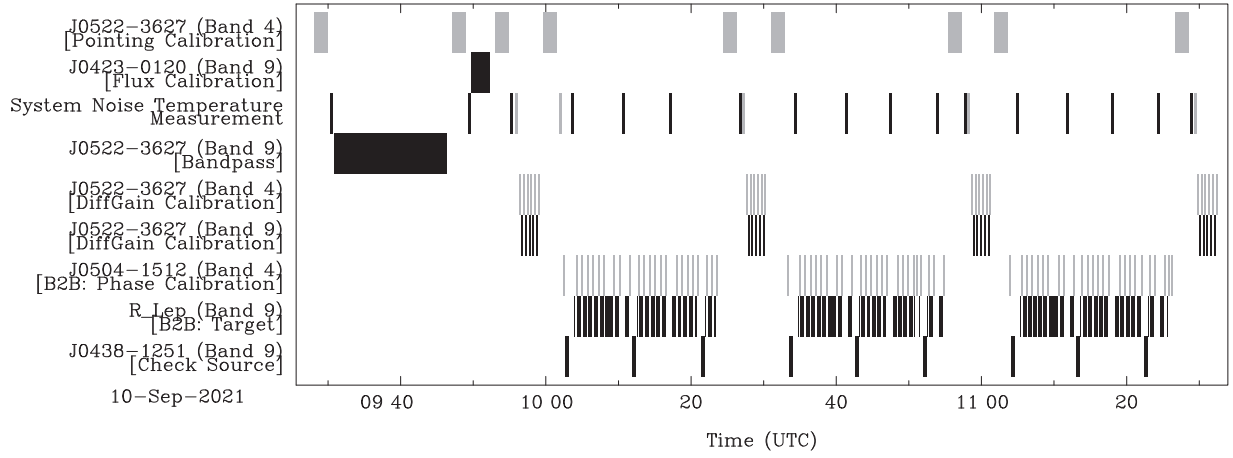
## 2. Experiments

### 2.1. Overview

The ALMA long baseline imaging capability in Bands 8–10 was demonstrated in HF-LBC-2021 by observing R Lep. In the experiments, the quasar J0504-1512, whose separation angle from R Lep is  $1''.2$ , was selected as the phase calibrator. One experiment run was performed in each of Bands 8–10 and the parameters for the three experiments are listed in Table 1. Note that the experiment codes B-08–B-10 indicate the observing frequencies in Bands 8–10, respectively. Table 2 lists the other calibrators and check sources (quasars used to independently assess the data quality). A 10 minute bandpass scan on a bright quasar was placed at the beginning of the experiment as shown in Figure 1. This scan determines the amplitude and phase change as a function of frequency for each of the HF spectral windows, and is then applied to all scans in the experiment, as per standard bandpass calibration for all ALMA data.

In Band 8 we set up two HF spectral windows each with a bandwidth of 1.875 GHz (frequency width per channel of 976.56 kHz) and the other two HF spectral windows with a bandwidth of 2 GHz (frequency width per channel of 15.625 MHz), as listed in Table 3. In Bands 9 and 10, we used eight HF spectral windows with a bandwidth of 1.875 GHz (frequency width per channel of 976.56 kHz), made possible with  $90^\circ$  Walsh phase switching to enable sideband separation in the double sideband receiving systems (Emerson 2005). Each spectral window was observed in the two linear polarization pairs, called  $XX$  and  $YY$ . In Band 10, one of the spectral windows covered the HCN maser at 890.7607 GHz in the  $J = 10-9$  transition between the ( $11^1_0$ ) and ( $04^0_0$ ) vibrationally excited states.

Table 3 also lists low-frequency (LF) spectral windows used for B2B phase referencing. They were all acquired with single sideband receiving systems. In B-09 and B-10, two of the four LF spectral windows to observe were not available due to instrumental problems. These spectral windows were neither included in the data reduction, nor listed in Table 3.



**Figure 1.** Experiment schedule of the B-09 B2B phase referencing test. Black bars represent HF band scans in Band 9, while gray bars represent LF band scans in Band 4. The horizontal axis is the experiment date and time in UTC. The observed sources, bands (in parentheses), and scan intents (in square brackets) are found in the left part of the panels.

**Table 3**  
Spectral Setting of Spectral Windows

| Base Band No.<br>(Front-end Sideband)<br>(1) | Frequency Channel Spacing<br>(MHz)<br>(2) | HF Band Frequency Range<br>(GHz)<br>(3) | LF Band Frequency Range<br>(GHz)<br>(4) |
|--|---|---|---|
| B-08   |   |   |   |
| BB-1 (LSB)                                   | 0.9766                                    | 397.071–398.946                         | 127.051–128.926                         |
| BB-2 (LSB)                                   | 15.625                                    | 399.142–400.876                         | 129.122–130.856                         |
| BB-3 (USB)                                   | 15.625                                    | 409.184–410.918                         | 139.164–140.898                         |
| BB-4 (USB)                                   | 0.9766                                    | 411.114–412.989                         | 141.094–142.969                         |
| B-09   |   |   |   |
| BB-1 (LSB)                                   | 0.9766                                    | 657.041–658.916                         | ...                                     |
| BB-1 (USB)                                   | 0.9766                                    | 675.000–676.875                         | ...                                     |
| BB-2 (LSB)                                   | 0.9766                                    | 658.916–660.791                         | ...                                     |
| BB-2 (USB)                                   | 0.9766                                    | 673.125–675.000                         | ...                                     |
| BB-3 (LSB)                                   | 0.9766                                    | 655.124–656.999                         | ...                                     |
| BB-3 (USB)                                   | 0.9766                                    | 676.917–678.792                         | 152.167–154.042                         |
| BB-4 (LSB)                                   | 0.9766                                    | 660.854–662.729                         | ...                                     |
| BB-4 (USB)                                   | 0.9766                                    | 671.188–673.063                         | 154.125–156.000                         |
| B-10   |   |   |   |
| BB-1 (LSB)                                   | 0.9766                                    | 884.629–886.504                         | ...                                     |
| BB-1 (USB)                                   | 0.9766                                    | 905.954–907.829                         | ...                                     |
| BB-2 (LSB)                                   | 0.9766                                    | 886.504–888.379                         | ...                                     |
| BB-2 (USB)                                   | 0.9766                                    | 904.080–905.955                         | ...                                     |
| BB-3 (LSB)                                   | 0.9766                                    | 888.379–890.254                         | ...                                     |
| BB-3 (USB)                                   | 0.9766                                    | 902.205–904.090                         | 302.827–304.702                         |
| BB-4 (LSB) <sup>a</sup>                      | 0.9766                                    | 890.254–892.129                         | ...                                     |
| BB-4 (USB)                                   | 0.9766                                    | 900.330–902.205                         | 304.785–306.660                         |

**Note.**

<sup>a</sup> The frequency range between 890.664 and 890.860 in Band 10 BB-4 (LSB) was excluded from the continuum imaging because of the HCN maser line.

**2.2. Goals of the Experiments**

The goals of our R Lep observations are to confirm that the observation setup, and calibration and image procedures for ALMA HF long baseline observations can achieve accurate and representative images of the science target source while following the below scenario:

- (1) Using B2B phase referencing,
- (2) Using a close phase calibrator,

- (3) Fast switching between the target and a phase calibrator, and
- (4) Assessing phase stability prior to execution using a “Go/NoGo” check.

In the case that the visibility phase includes random phase noise, the coherence factor of the visibilities,  $\eta$ , can be estimated as follows:

$$\eta = \exp[-\sigma_{\Phi}^2/2], \tag{1}$$

where  $\sigma_{\phi}$  is the standard deviation of the interferometric phase noise (Thompson et al. 2017, Section 13.1.6). In general, synthesized images generated by Fourier transforming point-source visibilities suffer from an image peak degradation equivalent to Equation (1) due to random phase noise that we characterize as a ratio of the obtained image peak to that of the true brightness distribution convolved with the synthesized beam. We refer to this as the image coherence. In our previous studies image structure defects are minimal to negligible for point sources with a 70% image coherence and under these conditions, we therefore expect images of science targets to be accurate and representative (M20; M22).

Although R Lep may have an extended structure, we also apply these criteria to the HF-LBC-2021 experiments, in that we ensure good phase stability before observing and maintain a low residual phase rms for the target after B2B phase referencing by using a close phase calibrator. For R Lep we assume that the beam-convolved true brightness distribution can be retrieved by self-cal as discussed in Section 3.5, and thus we can measure the image coherence by comparing an image made after B2B phase referencing with those made after self-cal. In the following subsections, the application of the above techniques and criteria in order to achieve an image coherence of  $\geq 70\%$  are described.

### 2.2.1. B2B Phase Referencing

For most HF experiments, especially in Bands 9 and 10, pointlike quasars lying within a suitable angular separation from the target source will not be always bright enough to provide robust phase solutions. However, since the flux densities of quasars often increase at lower frequencies, it is possible to apply the solutions derived at lower frequencies to the higher frequency data using the B2B phase referencing. As detailed in Maud et al. (2023b), irrespective of using in-band or B2B phase referencing, the calibrator separation angle to the target should be  $\sim 1^\circ$  in Bands 9 and 10 before using the longest baseline configuration. Only when using B2B phase referencing for R Lep does the quasar J0504-1512, at  $1^\circ.2$ , meet the separation angle requirement. In the following descriptions, the observing band used for the target is referred to as an HF band with the HF representative frequency of  $\nu_{\text{HF}}$ . The lower frequency band used to observe the phase calibrator is referred to as an LF band with the LF representative frequency of  $\nu_{\text{LF}}$ . The LF band spectral setup is automatically determined by the ALMA observatory control software (ALMA online software) to minimize the system overheads incurred when frequency switching between the HF and LF bands to  $\sim 2$  s by using a harmonic frequency switching method (A20; Shillue et al. 2012).

In the data reduction, the antenna-based phase of the phase calibrator at  $\nu_{\text{LF}}$  with respect to a reference antenna is scaled to  $\nu_{\text{HF}}$  by multiplying by the frequency ratio,  $R = \nu_{\text{HF}}/\nu_{\text{LF}}$ . This scaling is relevant if the variable phases are associated with delays in each antenna path, such as those caused by the troposphere, antenna position error and other common instrumental paths between the antenna and the correlator. See A20 for more details.

There is also an additional instrumental phase offset, independent of the frequency scaling, that exists between the HF and LF spectral windows. These phase offsets (one for each spectral window) are calibrated by observing a strong quasar,

called the Differential Gain Calibration (DGC) source, while alternating very rapidly between the HF and LF bands such that atmospheric variations are corrected and the remaining phase offset can be determined (A20). For each of the three R Lep experiments, four DGC sequences were used to determine if the spectral window phase offsets were constant over each experiment. The observing sequence of B-09 is depicted in Figure 1. As noted by A20, the DGC source does not need to be close to the science target, although it must be bright so that the frequency switching scans can be made faster than the switching cycle between the target and phase calibrator. In the experiments, the DGC source used was J0522-3627, which has an angular separation from the target of  $22^\circ.3$ , and a flux density of  $>4$  Jy in the HF bands (see Section 3.2), and so it is sufficiently strong. However, it is not a perfect point source (Leon et al. 2016), and the possible effect of its structure on obtaining the spectral window phase offsets is discussed in Section 5.2.

### 2.2.2. Antenna Fast Switching and the Go/NoGo Check

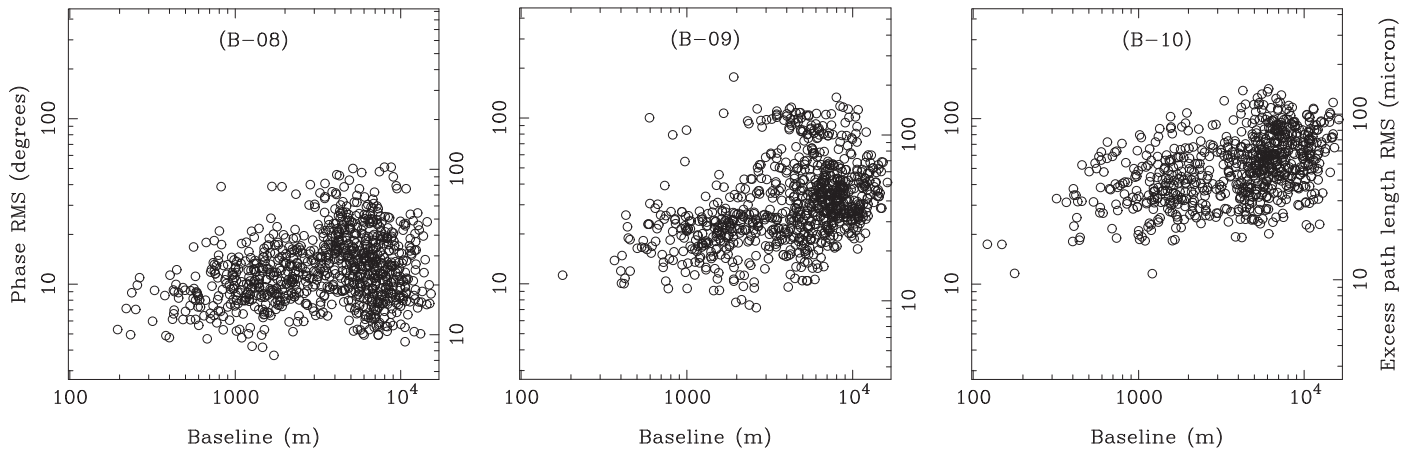
Short timescale atmospheric phase fluctuations affect the phase stability even in low precipitable water vapor (PWV) conditions (Asaki et al. 2016; Matsushita et al. 2017; Maud et al. 2017, 2023a). In order to reduce the fast phase variations in ALMA phase referencing observations, while retaining adequate target on-source time, we chose the switching cycle time  $t_{\text{swt}}$  to be 50 s. The target scan length was  $\sim 31$  s and the phase calibrator scan length was  $\sim 13$  s, with an overhead of  $\sim 6$  s to change the antenna pointing and receiver band. We imposed the nominal ALMA limits on the amount of PWV of 0.91, 0.66, and 0.47 mm for the experiments in Bands 8–10, respectively.

Just before each experiment, we conducted a 120 s short observation of a bright quasar, J0423-0120, to check the atmospheric phase stability by measuring the phase rms at an arbitrary frequency  $\nu_{\text{GNG}}$  available at that moment. This short observation is referred to as a Go/NoGo check in this paper. We derived the phase rms at  $\nu_{\text{HF}}$  by scaling by the ratio between  $\nu_{\text{GNG}}$  and  $\nu_{\text{HF}}$ . Note that ALMA operators monitor visibility phases corrected with solutions derived from Water Vapor Radiometer (WVR) measurements (Nikolic et al. 2013) using the ALMA online calibration software TELCAL (Broggière et al. 2011). In general, the phase rms is proportional to the square root of the observation interval (M22). The B2B phase referencing experiments have a switching cycle time of  $\sim 50$  s, giving a time scaling factor of  $[120 \text{ s}/50 \text{ s}]^{0.5} = 1.54$ . Using the phase rms of the Go/NoGo check, we can predict the image coherence from a modified coherence factor  $\eta'$  based on Equation (1) as follows:

$$\eta' = \exp[-(\nu_{\text{HF}}/\nu_{\text{GNG}})^2(\sigma_{\text{GNG}}/1.54)^2/2], \quad (2)$$

where  $\sigma_{\text{GNG}}$  is the median phase rms using the longest quartile of baseline lengths from the Go/NoGo check at  $\nu_{\text{GNG}}$ . Given our aim to achieve an image coherence of  $\geq 70\%$ , we required  $(\nu_{\text{HF}}/\nu_{\text{GNG}})\sigma_{\text{GNG}} \leq 0.8$  rad ( $=45^\circ$ ) for the longest quartile of baseline lengths (M22).

Figure 2 shows the phase rms as a function of the baseline length of the Go/NoGo checks, and Table 4 lists the weather conditions obtained from the Go/NoGo checks. The modified coherence factors calculated from Equation (2) are 95%, 85%, and 77% for the conditions of B-08–B-10, respectively. Further



**Figure 2.** Rms phase as a function of baseline length of the 120 s Go/NoGo checks for J0423-0120 just before the experiments. The horizontal axis denotes the baseline length, and each open circle denotes the phase rms value in degrees at  $\nu_{\text{HF}}$  for a single baseline. The flux density of J0423-0120 was bright (6.4, 3.4, and 2.6 Jy at Bands 3, 7, and 9, respectively) and the thermal phase noise is negligible after averaging the available spectral windows and the dual polarization pairs. Note that the corresponding excess path length rms is expressed in the second vertical axis in microns at the right side.

**Table 4**  
HF-LBC-2021 Go/NoGo Check before Starting the Experiment

| Exp Code | Source     | Band Frequency<br>(GHz) | PWV<br>(mm) | Phase rms at $\nu_{\text{HF}}$<br>(top quartile) | Excess Path Length rms<br>( $\mu\text{m}$ ) (top quartile) | Execution Block<br>(uid://A002/) |
|----------|------------|-------------------------|-------------|--|--|----------------------------------|
| (1)      | (2)        | (3)                     | (4)         | (5)  | (6)  | (7)                              |
| B-08     | J0423-0120 | Band 3 (103)            | 1.01        | 28°  | 57   | Xf0e992/X4d02                    |
| B-09     | J0423-0120 | Band 4 (140)            | 0.29        | 50°  | 63   | Xf07268/X317e                    |
| B-10     | J0423-0120 | Band 7 (350)            | 0.28        | 63°  | 59   | Xf06573/X2087                    |

discussions about the relation between the Go/NoGo check and the actual image coherence are presented in Section 5.1.2.

### 3. Data Reduction

The data reduction was carried out using custom data reduction scripts generated by the ALMA calibration script generator (Petty et al. 2014)<sup>15</sup> based on the Common Astronomy Software Applications (CASA; Bean et al. 2022). As per standard procedures, the ALMA cross-correlated data, or in other words, Archival Science Data Models were converted to a CASA MeasurementSet (MS). Thereafter, we applied conventionally derived corrections such as WVR phase corrections (Nikolic et al. 2013; Matsushita et al. 2017), any updated antenna positions, and HF bandpass calibration to the MSs. In all such experiments, it is important that accurate antenna positions are used (Hunter et al. 2016; Maud et al. 2023b). For the LF bandpass calibration, we made use of the LF DGC scans of J0522-3627 as listed in Table 2.

#### 3.1. Phase Calibration

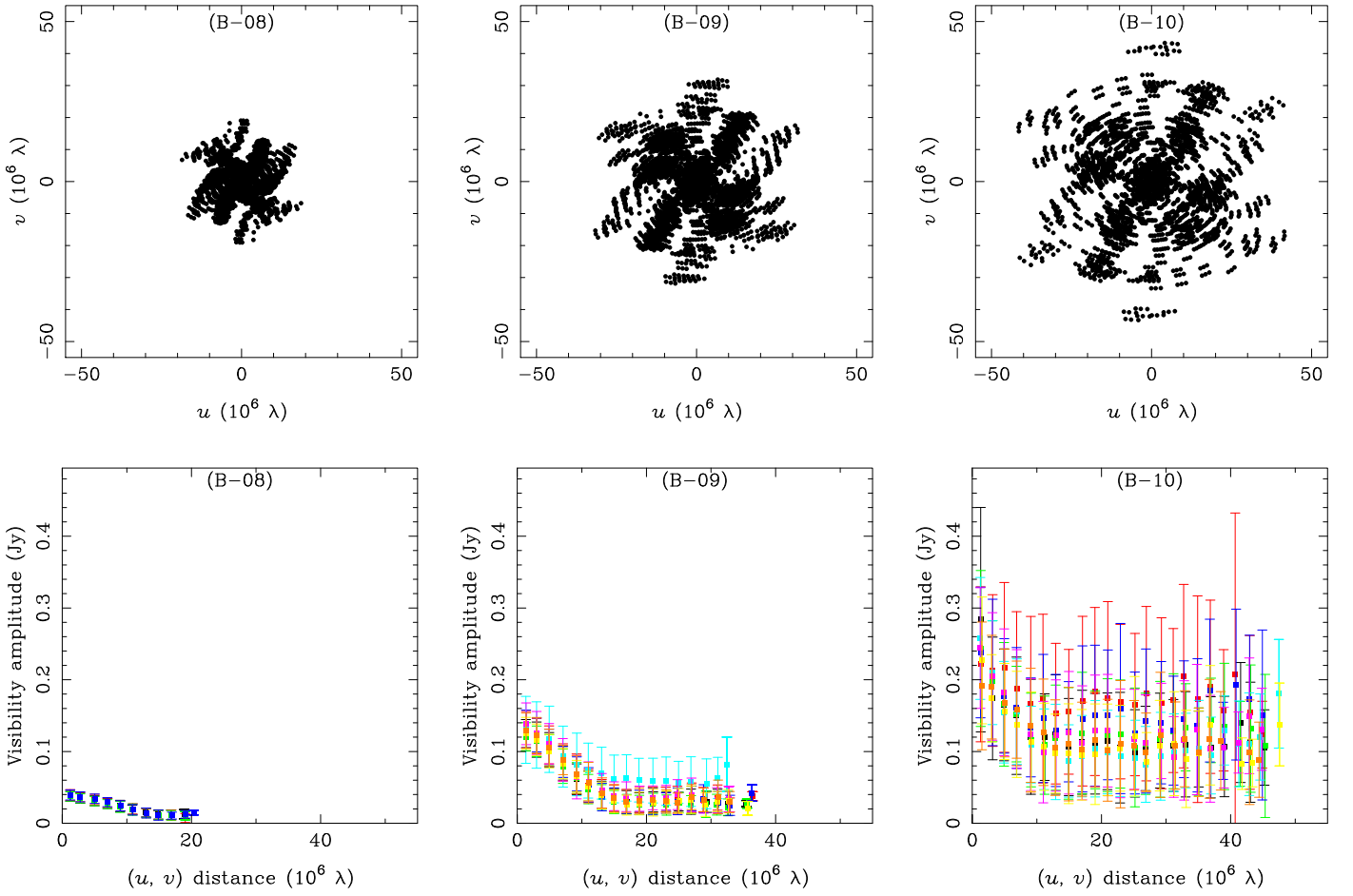
There are three stages in our data reduction for B2B phase referencing. The first stage is the elimination of the instrumental phase offsets between the LF spectral windows; the second is the estimation of the instrumental phase offset for the HF spectral windows with respect to the LF band; and the final stage is applying the LF phase calibrator solutions using B2B phase referencing to correct the HF target phases. At the first stage (corresponding to step (a) in A20, Figure 3), we

obtained time-averaged LF band phase solutions for the DGC source J0522-3627 for each LF spectral window for each polarization pair. This set of DGC solutions is referred to as the LF DGC offset. For B-08, there are four LF (Band 4) spectral windows, each with two polarization pairs, and therefore we obtained in total eight LF DGC offsets (four spectral windows  $\times$  two polarization pairs). On the other hand, for B-09 and B-10, there are two LF spectral windows available (Bands 4 and 7, respectively); therefore, we obtained four LF DGC offsets for each band. In the next step, the LF DGC offsets were subtracted from the corresponding LF spectral windows (steps (b) and (e) in A20, Figure 3).

In the second stage, we derived time-dependent phase solutions for the DGC at  $\nu_{\text{LF}}$  for each scan. In B-09 and B-10 the solutions were averaged for both LF spectral windows to improve the signal-to-noise ratio (S/N). These solutions are referred to as the LF DGC solutions. The solutions were interpolated in time and extrapolated in frequency (by multiplying by the frequency ratio  $R$ ), and applied to the HF DGC spectral windows, to calibrate short timescale atmospheric phase fluctuations in the HF DGC scans (step (c) in A20, Figure 3). This calibration essentially removes the temporal phase fluctuations and leaves only the offset between LF and HF spectral windows. Thus, in applying these corrections, we derive a time-averaged solution including scans per group of the HF DGC repeats (step (d) in A20, Figure 3), producing eight and 16 HF DGC offsets in Band 8, and Bands 9 and 10, respectively, one for each spectral window for each polarization pair.

At the final stage, we derived per scan phase solutions for the LF phase calibrator J0504-1512. For B-09 and B-10, we combined the two LF spectral windows to improve the S/N, while for B-08 the individual spectral windows were solved separately. The HF

<sup>15</sup> The utility module of the script generator can be downloaded from Hunter et al. (2023).



**Figure 3.** Top:  $(u, v)$  coverage of R Lep in B-08–B-10 from the left, middle, and right, respectively. Bottom: visibility amplitude of the continuum as a function of  $(u, v)$  distance of R Lep in B-08–B-10 from the left, middle, and right, respectively. The visibility data were first vector averaged in time and two polarization pairs. Then the data are scalar averaged in each  $2 \text{ M}\lambda$  bin. The color represents each spectral window. In Band 9, one of the spectral windows in BB-3 (LSB; light blue color) has a systematically higher amplitude and deviation compared to the other spectral windows because a cluster of atmospheric  $\text{O}_3$  absorption lines exists (Pardo et al. 2022) in the bandwidth.

DGC offsets were applied to the corresponding HF spectral windows to remove the instrumental phase offset, and thereafter the application of the scaled-up scan-based LF phase calibrator solutions are used to calibrate the HF target phases. The LF phase solutions were interpolated in time and extrapolated in frequency by multiplying  $R$  (step (f) in A20, Figure 3).

### 3.2. Amplitude Calibration

The amplitude calibration procedure for the experiments followed the ALMA standard amplitude calibration flow (Cortes et al. 2022). As displayed in Figure 1,  $T_{\text{sys}}$  measurement scans in the HF band were inserted roughly every 8 minutes and the derived corrections were applied to the data. Although the LF  $T_{\text{sys}}$  measurement is needed neither for the HF target phase nor amplitude calibrations, LF band amplitude correction with  $T_{\text{sys}}$  was also made for checking the synthesized images of the LF calibrators.

The amplitude time variation of the HF spectral windows was determined using the DGC sequences in the HF band. The flux density scaling of R Lep was finally made by referring to the HF flux density of J0522-3627, whose Band 3 and 7 flux densities have been measured in ALMA’s grid source monitor (Fomalont et al. 2014; van Kempen et al. 2014; Farren et al. 2021). Assuming that the flux density is proportional to  $\nu^\alpha$ ,

where  $\nu$  is the observing frequency and  $\alpha$  is the spectral index determined between Bands 3 and 7, the flux density of J0522-3627 extrapolated to Bands 8–10 was 4.481, 4.390, and 4.137 Jy at 405, 667, and 896 GHz, respectively. The obtained spectral index, computed flux densities of J0522-3627, and the measurement epochs are listed in Table 5. The ramifications of the slight structure in J0522-3627 are discussed in Section 5.2.

### 3.3. Visibility Amplitude Analysis of the Continuum Source

The top panels of Figure 3 show the  $(u, v)$  coverage of the R Lep target scans normalized by the wavelength. The maximum  $(u, v)$  distance is 20, 36, and  $48 \text{ M}\lambda$  in Bands 8–10, respectively, corresponding to angular scales of 10, 5.8, and 4.3 mas. Note that the 80th percentile of the  $(u, v)$  distance is 9.4, 19, and  $25 \text{ M}\lambda$  in Bands 8–10, respectively, corresponding to angular scales of 22, 11, and 8.3 mas. These divergences between the maximum and 80th percentile  $(u, v)$  distance are caused by nonuniformly distributed  $(u, v)$  coverage. In the following synthesis imaging using CASA `tclean` we set the customary weighting of visibility samples (“Briggs” robustness parameter of 0.5) to optimize ALMA imaging fidelity.

The bottom panels of Figure 3 show the calibrated visibility amplitude of the continuum emission as a function of  $(u, v)$

**Table 5**  
Flux Density and Spectral Index of J0522-3627 Measured in the ALMA Grid Source Monitor

| Exp Code | Frequency<br>(GHz) | Spectral Index | Calculated Flux Density<br>(Jy) | Measurement Epoch<br>(Band 3) | Measurement Epoch<br>(Band 7) |
|----------|--------------------|----------------|---------------------------------|-------------------------------|-------------------------------|
| (1)      | (2)                | (3)            | (4)                             | (5)                           | (6)                           |
| B-08     | 405.0              | -0.331         | 4.481                           | 2021 Sep 21 and 26            | 2021 Sep 11 and 25            |
| B-09     | 667.0              | -0.253         | 4.390                           | 2021 Sep 9 and 11             | 2021 Sep 10                   |
| B-10     | 896.2              | -0.250         | 4.137                           | 2021 Sep 9                    | 2021 Sep 3 and 10             |

**Table 6**  
Elliptical Disk Fitting Result of the  $(u, v)$  Visibility Data of R Lep

| Exp Code | Flux Density<br>(mJy) | Position Offset <sup>a</sup><br>( $\Delta\alpha \cos \delta, \Delta\delta$ ) (mas) | Source Size<br>Major Axis $\times$ Minor Axis (mas) | Source Position<br>Angle (deg) |
|----------|-----------------------|--|---|--------------------------------|
| (1)      | (2)                   | (3)  | (4)   | (5)                            |
| B-08     | $37.3 \pm 0.1$        | (-0.0, 0.8)  | $14.2 \times 14.2$                                  | ...                            |
| B-09     | $106.9 \pm 0.5$       | (-0.1, 0.5)  | $16.3 \times 15.6$                                  | 31                             |
| B-10     | $179.9 \pm 1.7$       | (0.1, 1.2)   | $18.1 \times 18.1$                                  | ...                            |

**Note.**

<sup>a</sup> The origin is at the phase tracking center of R Lep.

distance. The first NULL point in the visibility amplitude appears at  $\sim 15$  M $\lambda$  in Bands 8 and 9, while it is not as clearly seen in Band 10, due to the higher noise level relative to the other bands. Beyond this point, the amplitude remains low in Bands 8 and 9, and probably also in Band 10. Assuming that the morphology of the brightness distribution of the continuum source of evolved stars is well represented by a uniform disk at these frequencies (Matthews et al. 2018; Vlemmings et al. 2019), we fitted the visibilities to a disk model using CASA `uvmodelfit`. The fitting results are listed in Table 6. The continuum emission has a more extended distribution of 14–18 mas than the synthesized beam sizes. This will be discussed in Section 3.5.1 in relation to self-cal.

### 3.4. Imaging for R Lep in the HF Bands

After the phase and amplitude calibration including B2B phase referencing, images were synthesized for R Lep with an imaging area of  $512 \times 512$  mas<sup>2</sup> with a pixel size of 1 mas, centered at (04<sup>h</sup>59<sup>m</sup>36<sup>s</sup>.3590,  $-14^\circ 48' 22''.531$ ) in ICRS. CASA `tclean` was used for imaging with a Briggs robustness parameter of 0.5 and a small cleaning box around the compact source at the center of the image. For the continuum images in Bands 8 and 9, the entire frequency range was used, whereas for Band 10 the known frequency range of the HCN maser emission, between 890.664 and 890.860 GHz, was excluded.

For the Band 10 HCN maser, we subtracted the continuum emission from the spectral channels containing the HCN maser line using a linear fit to the calibrated visibilities in the surrounding channels in the corresponding spectral window (BB-4 LSB). The frequency axis was adjusted to the local standard of rest Kinematic (LSRK) frame with respect to the rest frequency of the HCN maser line. Those two procedures were made at once using CASA `mstransform`. An image cube of the HCN maser emission was made covering 100 channels, centered at 890.742 GHz, each with a frequency width of 976.562 kHz. This corresponds to a velocity width of  $\sim 0.3$  km s<sup>-1</sup>.

### 3.5. Self-cal

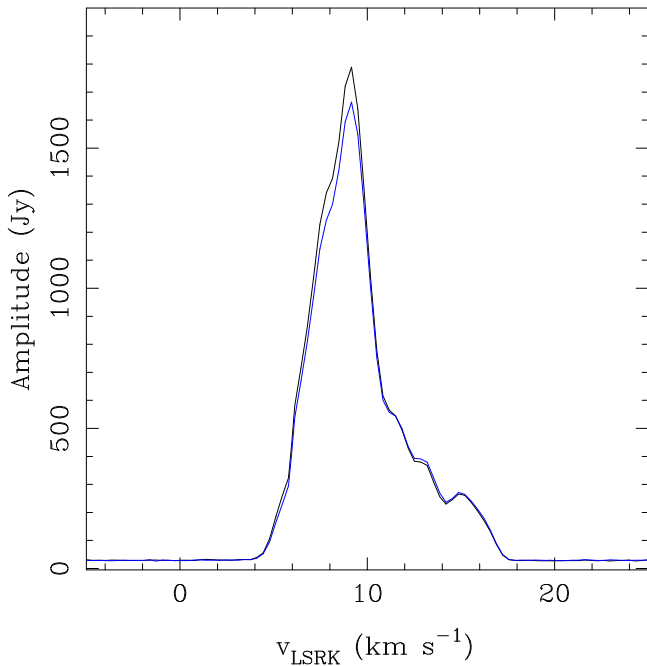
In order to estimate the percentage of image coherence achieved using B2B phase referencing, we need to compare these images with the best possible target images, achieved using self-cal. The introduction of self-cal is covered by Pearson & Readhead (1984; see also Bean et al. 2022 and references therein). Self-cal uses CLEAN components from a phase-referenced image as a model. Their Fourier transform is compared with the observed visibilities to derive corrections (mainly to the phase variations caused by the troposphere during the target source scans), that when applied can lead to an improved image which may in turn be used in further rounds of self-cal as the coherence is step-wise improved. Brogan et al. (2018) and Richards et al. (2022) describe recent implementations of self-cal for ALMA data reduction. The measured image coherence is described in detail in Section 5.

#### 3.5.1. Continuum Self-cal

The CLEANed continuum images of R Lep obtained after applying B2B phase referencing were used to provide the CLEAN component models to the “MODEL” column of the MSs for one round of phase self-cal. The target scan length (25–30 s on average) was used as the solution interval. We assumed that the continuum emission is unpolarized and, within each ALMA band, there are negligible changes in its structure and angular extent, such that we combined the *XX* and *YY* polarization pairs and all the spectral windows to increase the S/N. In all cases, when applying the self-cal corrections, if the solution for a particular antenna and scan had failed, the corresponding data were flagged.

Self-cal decomposes per-baseline solutions into corrections applied per antenna, so a minimum S/N (usually 3) is required for each antenna, per solution interval. In Band 8, the continuum emission extends over only a factor of  $\sim 1.5$  of the synthesized beam, so there was good S/N on all baseline lengths, and accurate phase self-cal solutions were obtained for almost all antennas and scans. A negligible amount of data was





(B-10: B2B phase referencing+HCN maser self-cal)

**Figure 4.** Cross-correlation spectrum for the HCN maser at 890.8 GHz, from the  $J = 10-9$  transition between the  $(11^1_0)$  and  $(04^0_0)$  vibrationally excited states, for the shortest projected baseline antenna pair with the  $(u, v)$  distance of 5259–5290 k $\lambda$ . The horizontal axis represents the radial velocity in  $v_{\text{LSRK}}$  (kilometers per second), and the vertical axis represents the cross-correlated flux density (jansky). The black and blue lines represent the  $XX$  and  $YY$  polarization pairs, respectively. The line profile was obtained by scalar averaging in time.

flagged due to failed solutions so the synthesized beam sizes are very similar before and after phase self-cal.

For Bands 9 and 10 the continuum source extends over 3–5 synthesized beams and the S/N on baselines to the most distant antennas was too low to provide calibration solutions in self-cal: good solutions were only obtained for the antennas contributing shorter baselines. In applying the corrections, much of the data were flagged due to failed solutions, so this led to a lower angular resolution for the images made after self-cal as the longest  $(u, v)$ -distance spacings had been removed.

The synthesized beam widths after continuum self-cal were changed by factors of 1.0, 1.6, and 3.7 in Bands 8–10, respectively. We therefore took the data for each band with only B2B phase referencing applied and flagged the same antennas/scans as were lost due to the failed solutions in continuum self-cal. This enabled us to make target images at the same resolution as the continuum self-cal images, in order to compare the recovered flux and assess the image coherence with B2B phase referencing alone.

### 3.5.2. Band 10 HCN Maser Self-cal

Figure 4 shows the detected HCN maser cross-correlated spectrum for a pair of antennas with the shortest projected baseline length of 5259–5290 k $\lambda$ . As is indicated from the line profile, creating the HCN maser cube confirmed that the brightest HCN maser emission was located in the spectral channel at the LSRK velocity of 9.4 km s $^{-1}$  and that the peak emission region was spatially compact. The image model of this single channel was used for phase self-cal with the solution interval of  $\sim 6$  s (approximately the correlator data integration

period). This produced an improved HCN maser image at the LSRK velocity of 9.4 km s $^{-1}$ , and this model was then used for amplitude self-cal with the solution interval of the scan length (25–30 s). These phase and amplitude self-cal corrections were then applied to the entire Band 10 HCN maser as well as the continuum data sets using CASA `applycal` with `interp='linearPD'` to each integration and scan without interpolating in time. This allowed imaging of the self-cal Band 10 R Lep HCN maser and the continuum emission at the full angular resolution.

## 4. Results

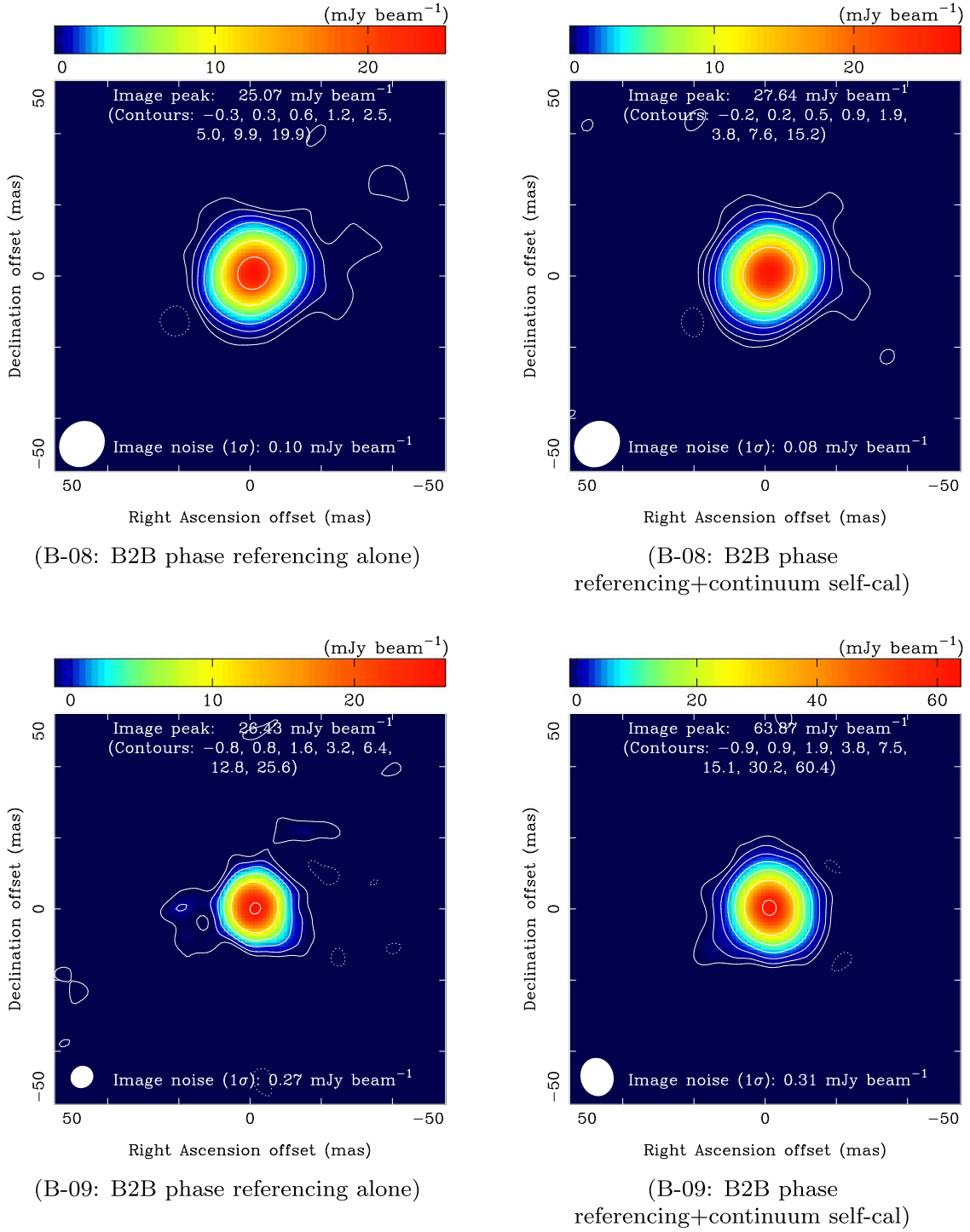
### 4.1. Image Coherence Using the Continuum Self-cal

The images of the continuum emission of R Lep with B2B phase referencing alone are shown in the left panels of Figure 5 in Bands 8 and 9, and the left panel of Figure 6 in Band 10. Table 7 summarizes image characteristics of the continuum images with B2B phase referencing alone including the beam size, image peak flux density, image rms noise, and the peak brightness temperature. These images are at the highest possible angular resolution in each HF band. The Band 10 image has a synthesized beam of  $4.9 \times 4.7$  mas, which is the maximum angular resolution that ALMA is capable of.

The images with B2B phase referencing and continuum self-cal (denoted, B2B phase referencing+continuum self-cal) are shown in the right panels of Figure 5 in Bands 8 and 9, and the middle panel of Figure 6 in Band 10. Table 8 summarizes the characteristics of the B2B phase referencing+continuum self-cal images. Because the longer baselines were flagged out especially in Bands 9 and 10 as explained in Section 3.5.1, the beam size of the B2B phase referencing+continuum self-cal became wider than that with B2B phase referencing alone. To align the beam size in each band and make the comparisons of the images between B2B phase referencing alone and B2B phase referencing+continuum self-cal, we made images with only B2B phase referencing applied but also the flags that occurred during the continuum self-cal that accordingly removed the longest  $(u, v)$ -distance spacings. The image coherence with B2B phase referencing alone but with the continuum self-cal flags in Bands 8–10 is 92%, 83%, and 77%, respectively, as listed in the last column of Table 8. The obtained image coherence for the continuum emission would be a representative value for array configurations with  $B_{\text{max}} \leq 16$  km, for Bands 9 and 10, while in Band 8 we obtained the high image coherence of 92% for the full 16 km scale array configuration. Considering the beam size of the B2B phase referencing+self-cal images, the effective longest baseline for the R Lep continuum source when doing continuum self-cal is  $\sim 10$  and  $\sim 5$  km in Bands 9 and 10, respectively.

### 4.2. Image Coherence in Band 10 Using the HCN Maser Self-cal

The image characteristics of the HCN maser at the LSRK velocity of 9.4 km s $^{-1}$  are listed in Table 7, and those of the HCN maser at the same velocity channel and the Band 10 continuum calibrated with B2B phase referencing+HCN maser self-cal are listed in Table 9. The right panel of Figure 6 shows the Band 10 continuum image calibrated with B2B phase referencing+HCN maser self-cal. Figure 7 shows the resultant cube made with B2B phase referencing+HCN maser self-cal

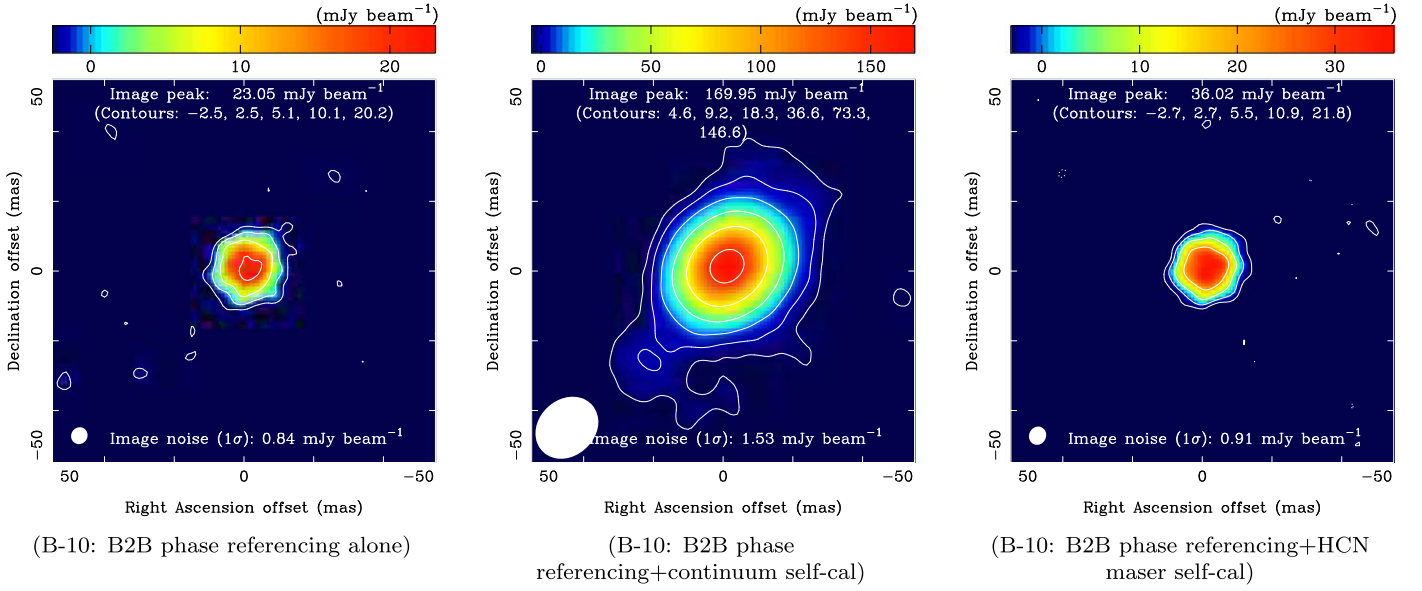


**Figure 5.** R Lep HF long baseline synthesized images for the continuum emission at Bands 8 and 9 in the top and bottom, respectively. The left and right panels are the images before and after phase self-cal (using the continuum), respectively. The solid line contours start from  $3\sigma$  level, increased by a factor of a power of 2, and the dashed line contour represents the  $-3\sigma$  level. The contour levels are shown on the upper side of each panel. The image peak value and rms noise are indicated at the top and bottom of each panel, respectively. The ellipse in the lower left represents the synthesized beam. Note that the synthesized beam size of the continuum self-cal image at Band 9 becomes broader compared to that of the original images because phase self-cal solutions were not obtained for some of the more distant antennas and the data for these were flagged in applying the solutions.

by averaging every four contiguous velocity channels in imaging, corresponding to a velocity width of  $1.3 \text{ km s}^{-1}$ . The averaged HCN maser emission in the velocity range between  $-4.4$  and  $21.6 \text{ km s}^{-1}$  is shown in Figure 8.

As mentioned in Section 4.1, we made images with only B2B phase referencing applied but also the HCN maser self-cal flags for the HCN maser at the LSRK velocity of  $9.4 \text{ km s}^{-1}$

and the Band 10 continuum. Because we could successfully obtain the self-cal solutions for the full  $(u, v)$  coverage, thanks to the compact and bright emission of the HCN maser, the beam size had little change after the HCN maser self-cal. The image peak flux density of the HCN maser at the LSRK velocity of  $9.4 \text{ km s}^{-1}$  changed from 735 Jy (Table 7 with B2B phase referencing alone) to 1247 Jy by self-cal afterward



**Figure 6.** R Lep Band 10 continuum image. Left: B2B phase referencing alone (before phase self-cal). Middle: after phase self-cal. Right: calibrated using the phase and amplitude self-cal solutions of the HCN maser channel at  $v_{\text{LSRK}} = 9.4 \text{ km s}^{-1}$ . The solid contours start from the  $3\sigma$  level, increased by a factor of a power of 2, and the dashed line contour denotes the  $-3\sigma$  level. The contour levels are shown on the upper side of each panel. The image peak value and rms noise are listed at the top and bottom of each panel, respectively. The ellipse in the lower left represents the synthesized beam. Note that the synthesized beam size of the middle, continuum phase self-cal image becomes broader compared to that of the original image (left panel) because the phase self-cal solutions were not obtained for some of the more distant antennas and the data for these were flagged in applying the solutions.

**Table 7**  
Image Characteristics of R Lep with Application of B2B Phase Referencing Alone

| Exp Code | Data Type              | Peak Flux Density<br>( $\text{mJy beam}^{-1}$ ) | Image rms Noise<br>( $\text{mJy beam}^{-1}$ ) | Synthesized Beam<br>Major Axis $\times$ Minor Axis<br>(mas) | Synthesized Beam<br>Position Angle<br>(deg) | Peak Brightness<br>Temperature (K) |
|----------|------------------------|---|---|---|---|------------------------------------|
| (1)      | (2)                    | (3)   | (4)   | (5)   | (6)   | (7)                                |
| B-08     | Continuum              | 25.1  | 0.1   | $13.6 \times 12.1$  | -42   | 1089                               |
| B-09     | Continuum              | 26.4  | 0.3   | $6.6 \times 6.1$  | -52   | 1750                               |
| B-10     | Continuum              | 23.0  | 0.8   | $4.9 \times 4.7$  | -33   | 1491                               |
| B-10     | HCN maser <sup>a</sup> | $735.2 \times 10^3$                             | $7 \times 10^3$                               | $5.6 \times 4.9$  | -19   | $40.73 \times 10^6$                |

**Note.**

<sup>a</sup> The original data cube with the velocity width of  $0.3 \text{ km s}^{-1}$  ( $v_{\text{LSRK}} = 9.4 \text{ km s}^{-1}$ ).

**Table 8**  
Image Characteristics of R Lep with Application of B2B Phase Referencing+Continuum Self-cal

| Exp Code  | Data Type | Peak Flux Density<br>( $\text{mJy beam}^{-1}$ ) | Image rms Noise<br>( $\text{mJy beam}^{-1}$ ) | Synthesized Beam<br>Major Axis $\times$ Minor Axis<br>(mas) | Synthesized Beam<br>Position Angle<br>(deg) | Peak Brightness<br>Temperature (K) | Image<br>Coherence<br>(%) |
|---|-----------|---|---|---|---|------------------------------------|---------------------------|
| (1)   | (2)       | (3)   | (4)   | (5)   | (6)   | (7)                                | (8)                       |
| B2B Phase Referencing+Continuum Self-cal                            |           |   |   |   |   |                                    |                           |
| B-08  | Continuum | 27.6  | 0.1   | $13.7 \times 12.2$  | -42   | 1187                               | ...                       |
| B-09  | Continuum | 63.9  | 0.3   | $10.8 \times 9.3$   | 13  | 1715                               | ...                       |
| B-10  | Continuum | 170.0   | 1.5   | $19.5 \times 16.1$  | -47   | 802                                | ...                       |
| B2B Phase Referencing Alone with Flags Caused by Continuum Self-cal |           |   |   |   |   |                                    |                           |
| B-08  | Continuum | 25.5  | 0.1   | $13.9 \times 12.4$  | -41   | 1060                               | 92                        |
| B-09  | Continuum | 52.9  | 0.4   | $10.8 \times 9.3$   | 13  | 1399                               | 83                        |
| B-10  | Continuum | 130.7   | 1.7   | $19.5 \times 16.1$  | -47   | 617                                | 77                        |

(Table 9). Thus, the image coherence at the brightest HCN maser velocity channel is 61% with B2B phase referencing alone. For the Band 10 continuum emission, we find that the image coherence achieved using B2B phase referencing was

70%. The image rms noise of the Band 10 continuum slightly increased from 0.8 to  $1.0 \text{ mJy beam}^{-1}$  after applying the flags of the HCN maser self-cal. We attribute this to the reduction of the number of visibilities. After applying B2B phase

**Table 9**  
Image Characteristics of R Lep with Application of B2B Phase Referencing+HCN Maser Self-cal

| Exp Code  | Data Type              | Peak Flux Density<br>(mJy beam <sup>-1</sup> ) | Image rms Noise<br>(mJy beam <sup>-1</sup> ) | Synthesized Beam<br>Major Axis × Minor Axis<br>(mas) | Synthesized Beam<br>Position Angle<br>(deg) | Peak Brightness<br>Temperature (K) | Image<br>Coherence<br>(%) |
|---|------------------------|--|--|--|---|------------------------------------|---------------------------|
| (1)   | (2)                    | (3)  | (4)  | (5)  | (6)   | (7)                                | (8)                       |
| B2B Phase Referencing+HCN Maser Self-cal                            |                        |  |  |  |   |                                    |                           |
| B-10  | HCN maser <sup>a</sup> | 1247 × 10 <sup>3</sup>                         | 3 × 10 <sup>3</sup>                          | 5.4 × 4.9  | −21   | 114.54 × 10 <sup>6</sup>           | ...                       |
| B-10  | Continuum              | 36.0   | 0.9  | 5.3 × 4.8  | −27   | 2065                               | ...                       |
| B2B Phase Referencing Alone with Flags Caused by HCN Maser Self-cal |                        |  |  |  |   |                                    |                           |
| B-10  | HCN maser <sup>a</sup> | 757.5 × 10 <sup>3</sup>                        | 7 × 10 <sup>3</sup>                          | 5.6 × 5.0  | −26   | 41.84 × 10 <sup>6</sup>            | 61                        |
| B-10  | Continuum              | 25.4   | 1.0  | 5.3 × 4.8  | −27   | 1457                               | 70                        |

**Note.**

<sup>a</sup> The original data cube with the velocity width of 0.3 km s<sup>-1</sup> ( $v_{\text{LSRK}} = 9.4 \text{ km s}^{-1}$ ).

referencing+HCN maser self-cal, the image rms noise is reduced down to 0.9 mJy beam<sup>-1</sup>, improving the image S/N from 29 to 40.

The image coherence of the Band 10 continuum image calibrated with B2B phase referencing alone of 70% is also larger than the 61% achieved on the single channel for the HCN maser. We attribute this to the fact that the continuum emission is centrally focused, whereas the HCN maser emission forms a ring structure wherein the distribution of flux distribution changes slightly before and after self-cal, i.e., we are applying a rule to measure image coherence for pointlike sources to something that has an extended distribution.

#### 4.3. Effectiveness of Continuum Self-cal for R Lep

Richards et al. (2022, Section 4.4.2) describe an analytical relation in self-cal between the solution interval, the number of antennas, and S/N. Applying their analysis to the initial S/N of 29 of the Band 10 continuum image, the per antenna, per scan S/N is <2 for 43 antennas and 50 scans, so it is not surprising that not all antenna solutions succeeded (even if considering the ideal peak flux after applying the B2B phase referencing+HCN maser self-cal to the Band 10 continuum, 36.0 mJy beam<sup>-1</sup>, the S/N per antenna, per scan remains <2). The degraded angular resolution (wider synthesized beam) image obtained after continuum self-cal yields an image S/N >100 and thus provides an S/N per antenna, per scan of >3 for the number of antennas not flagged by failed solutions (Table 8). Hence, limiting the minimum S/N for the self-cal solutions is obeyed, and solutions on antennas below this are flagged. The Band 9 continuum S/N per antenna, per scan, is also slightly <3 at the start of self-cal, and hence we again lose longer baseline data, although not as many as for Band 10. We do not pursue low-S/N mitigation strategies for self-cal of the continuum such as described in, e.g., Richards et al. (2022, Section 5.10). We note that if using lower S/N limits for self-cal solutions it might have been possible to save some longer ( $u, v$ )-distance spacings at the expense of solution accuracy.

#### 4.4. Interpretation of the R Lep Images

The uniform disk fitting analysis shows the diameter of the R Lep continuum source is ~14–18 mas as listed in Table 6, corresponding to 3–4 au submillimeter stellar radius at the distance of R Lep. Vlemmings et al. (2019) found that O-rich

AGB stars have mm-wave radio atmospheres 15%–50% larger than the optical/IR stellar radius. C-rich stars have been less studied except for IRC+10216, where Matthews et al. (2018) suggest a similar relationship. Our measured diameter at 0.33 mm wavelength is ~20% larger than the IR diameter (Hofmann et al. 2005), consistent with expectations.

At the angular resolution of 5 mas (corresponding to a 2.4 au linear scale at the distance of R Lep) we can characterize the location of the HCN maser distribution as a ring-like morphology with a diameter of 10–60 au, surrounding the Band 10 submillimeter-wave continuum emission. The extent of the HCN maser regions was found to be ~10–30 au in V Hya and IRC+10216 (Wong 2019), and our imaging result for the HCN maser in R Lep supports those previous works. We confirm the previous prediction that the maser emission must originate from the innermost regions of the CSE due to the high energy level ( $E_{\text{low}}/k > 4200 \text{ K}$ ) of the HCN maser line (Schilke & Menten 2003). This is also consistent with the observations of other HCN maser lines, which indicate that they arise in the wind-acceleration regions of carbon-rich AGB stars (e.g., Lucas & Cernicharo 1989; Menten et al. 2018; Jesty et al. 2022). Scientifically, the high angular resolution images provided by these technical tests can be used to characterize the inner wind of R Lep and facilitate the study of different processes close to the star, such as shocks driven by stellar pulsation, dust formation, and wind acceleration (Höfner & Olofsson 2018), in unprecedented detail.

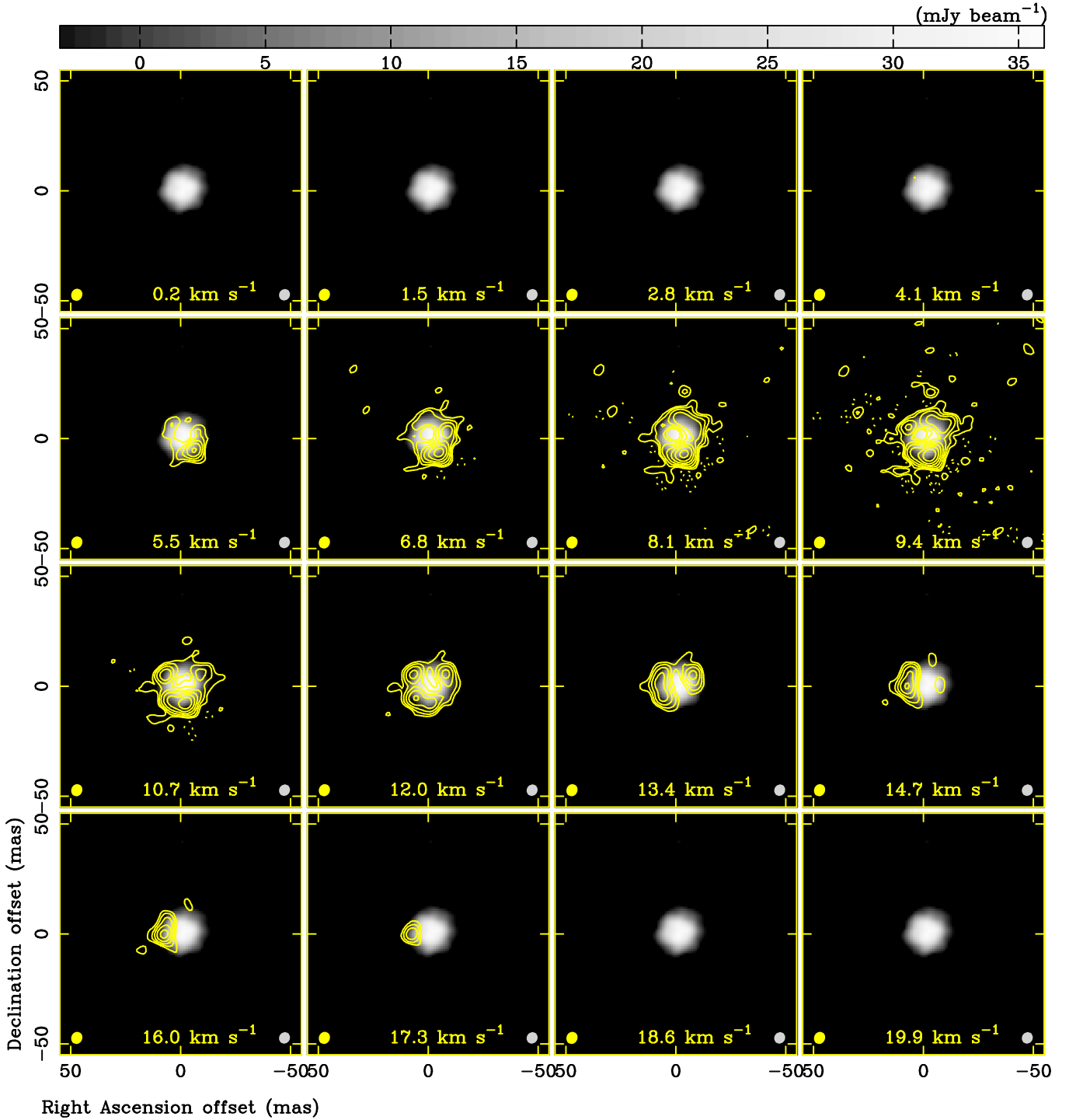
## 5. Discussion

### 5.1. Assessment of the Goals of the Experiments

Here we review the overarching goal of our experiments as described in Section 2.2, to achieve an image coherence of  $\geq 70\%$ .

#### 5.1.1. B2B Phase Referencing

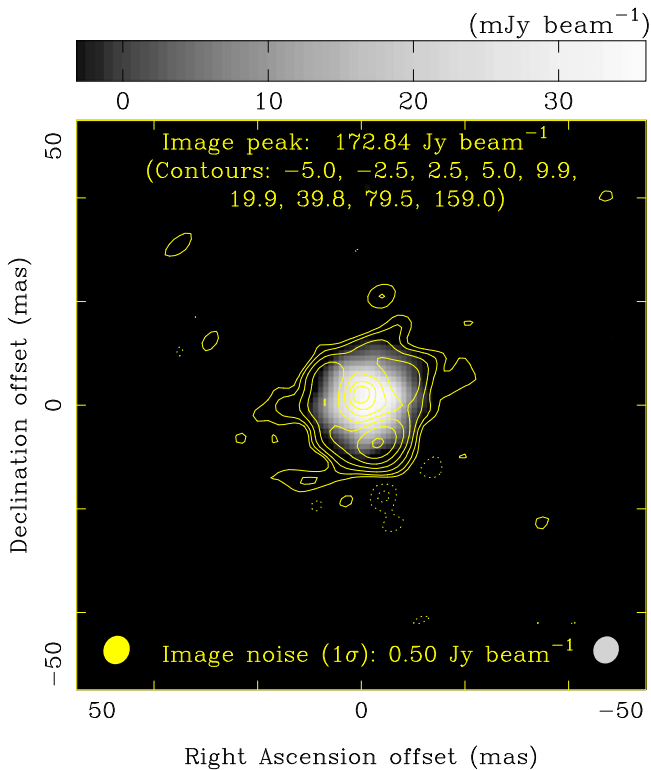
According to the ALMA calibrator source catalog, the phase calibrator J0504-1512 had the flux density of 0.15 and 0.10 Jy in Bands 3 and 7, respectively, in 2019 September, the most recent measurement at the time of our experiments. Assuming that the flux density is proportional to  $\nu^\alpha$ , the extrapolated flux density to Bands 8–10 is 0.09, 0.08, and 0.07 Jy, respectively, with the constant  $\alpha$  of  $-0.36$ . If we assume an in-band phase referencing scenario, using 43 12 m antennas with four, eight,



**Figure 7.** HCN maser cube in Band 10 (yellow contours) at 890.8 GHz, from the  $J = 10-9$  transition between the  $(11^1_0)$  and  $(04^0_0)$  vibrationally excited states, averaging every four velocity channels of the synthesized image cube with the velocity width of  $0.3 \text{ km s}^{-1}$ . The continuum emission in Band 10 is shown as a background grayscale gradation. The image cube was created after applying the amplitude and phase self-cal solutions derived using the HCN maser emission at  $v_{\text{LSRK}} = 9.4 \text{ km s}^{-1}$ . The image rms noise was calculated at each velocity channel from emission-free portions in the image. The minimum image rms noise is  $45 \text{ mJy beam}^{-1}$  in the channels with little maser emission at  $v_{\text{LSRK}} = 19.9 \text{ km s}^{-1}$ , and the maximum image rms noise is  $1787 \text{ mJy beam}^{-1}$  at  $v_{\text{LSRK}} = 9.4 \text{ km s}^{-1}$ . The solid line contours start from the  $5\sigma$  level per channel at  $v_{\text{LSRK}} = 9.4 \text{ km s}^{-1}$  ( $=8.9 \text{ Jy beam}^{-1}$ ), increased by a factor of a power of 2. The dashed line contours start from the  $-5\sigma$  level, increased by a factor of a power of 2. The contour levels are  $-17.8, -8.9, 8.9, 17.8, 35.6, 71.2, 142.4, 284.8,$  and  $569.6 \text{ mJy beam}^{-1}$ . The radial LSRK velocity is given at the bottom of each panel, and the synthesized beam size is shown on the lower left and right corners for the HCN maser ( $5.6 \times 5.0 \text{ mas}$ ) and continuum ( $5.3 \times 4.8 \text{ mas}$ ), respectively.

and eight 2 GHz bandwidth spectral windows in Bands 8–10, respectively, then even when combining the available spectral windows we can only achieve the S/Ns of 14, 6, and 3 in Bands 8–10, respectively, for a scan length of 13 s. Since the

required S/N for a single phase calibrator scan is 15 to provide qualified phase solutions, J0504-1512 is thus too weak to be detected with sufficient S/N in the short scan duration required for the fast switching phase calibration in Bands 9 and 10,



**Figure 8.** R Lep Band 10 HCN maser at 890.8 GHz, from the  $J = 10-9$  transition between the  $(11^1_0)$  and  $(04^0_0)$  vibrationally excited states, using the HCN maser cube averaged over the velocity range between  $-0.5$  and  $20.3 \text{ km s}^{-1}$  in the image cube with the velocity width of  $0.3 \text{ km s}^{-1}$  (yellow contours). The Band 10 continuum emission is shown as a background grayscale gradation. Phase and amplitude self-cal solutions for the HCN maser channel at  $v_{\text{LSRK}} = 9.4 \text{ km s}^{-1}$  were applied both to the HCN maser and the continuum data. The solid line contours start from the  $5\sigma$  level, increased by a factor of a power of 2. The dashed line contours start from the  $-5\sigma$  level, increased by a factor of a power of 2. The contour levels are shown on the upper side. The image rms noise of the continuum emission and HCN maser are  $0.9$  and  $497 \text{ mJy beam}^{-1}$ , respectively. The synthesized beam size is shown on the lower left and right corners for the HCN maser ( $5.4 \times 4.9 \text{ mas}$ ) and continuum ( $5.3 \times 4.8 \text{ mas}$ ), respectively.

while it could plausibly be used in Band 8. With in-band phase referencing we would have to search for a quasar brighter than  $572 \text{ mJy}$  in Band 10 (A20). The nearest quasar bright enough is J0522-3627 at the distant separation angle of  $22^\circ$ , in violation of the requirements stated by Maud et al. (2023b), and if used, it would mean that R Lep would not have been well calibrated (see Section 5.3). Hence, B2B phase referencing provides us with the only way to use J0504-1512 as the phase calibrator for Band 9 and 10 observations.

### 5.1.2. Antenna Fast Switching and Experiment Go/NoGo

The R Lep continuum images with B2B phase referencing alone compared to those with self-cal show that the image coherence in Bands 8–10 is 92%, 83%, and 77%, respectively (although with a degraded angular resolution for Bands 9 and 10, except when using the HCN maser self-cal where Band 10 achieved 70%). Meanwhile, the modified coherence factors obtained from the Go/NoGo checks (Equation (2)) were 95%, 85%, and 77%, respectively. Technically, the Go/NoGo check provides a prediction of the phase stability of a single source, hence providing the image coherence for in-band phase referencing with a  $0^\circ$  phase calibrator separation angle. However, a visibility phase error approximately proportional

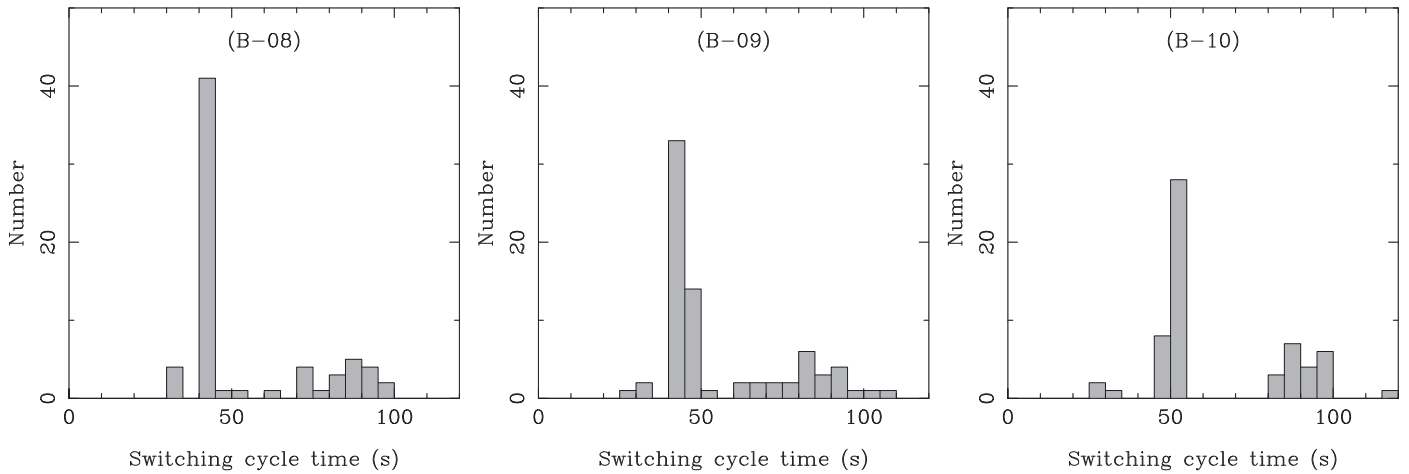
to the separation angle occurs in real observations (Maud et al. 2023b). In addition, M20 report that the image coherence in B2B phase referencing tends to be lower than that in in-band phase referencing because of the DGC process where a minor phase offset error can be propagated to the target visibility data. Although the Go/NoGo check cannot estimate the phase error propagation, the modified coherence factor is a reasonably good indicator in predicting the image coherence of these HF long baseline observations.

In the process of our experiments, we learned two important lessons related to achieving the required image coherence. First is the Go/NoGo phase rms condition. The phase rms of  $63^\circ$  in the B-10 Go/NoGo check was less stable than our “GO” criterion of  $45^\circ$  and is the very upper limit of what was acceptable. The worse-than-optimal stability conditions may be the main reason for the low image coherence in Band 10 compared to the other two bands. On the other hand, it is rare to find conditions better than our phase rms threshold even at the ALMA site. Recent analysis of the ALMA site weather conditions, in term of phase stability, show us that the fraction of suitable time meeting our low phase rms criteria is on average about 5%–10%, but it depends on the season: if we limit only to winter nights, the fraction is  $>10\%$  (Maud et al. 2023a). The same report also illustrates a higher fraction of time available with shorter switching cycle times, and hence in the future, our Go/NoGo threshold could be relaxed (increase) if we were to shorten  $t_{\text{swt}}$ , although at the expense of observational efficiency.

Second is the uneven distribution of the switching cycle times. Figure 9 shows a histogram of  $t_{\text{swt}}$ . Typically,  $t_{\text{swt}}$  is around 50 s in our experiments, while much longer gaps between phase calibration scans sometimes happened when the check source and/or  $T_{\text{sys}}$  measurement scans were inserted, as depicted in Figure 1. Thus, about a quarter to a third of the target scans had longer  $t_{\text{swt}}$  than 60 s in the experiments (Figure 9). Those scans were usable, but not ideal, because the longer  $t_{\text{swt}}$  means the phase calibration is not as optimal, and hence allows for a larger decoherence. The timing of the insertion of check source and  $T_{\text{sys}}$  measurement scans is controlled by the ALMA online software, which, as a result of our experiments, has been improved from Cycle 10 for HF long baseline observations, by putting those extra scans outside of the target and phase calibrator sequence in order not to cause longer  $t_{\text{swt}}$ .

### 5.2. Effect of Morphology of the Phase Calibrator and DGC Source on the Target Images

In the imaging of the phase calibrator (J0504-1512) and the DGC source (J0522-3627) we found low flux level minor extended structures. In general, if a phase calibrator has a resolved structure, applying its phase solutions to the target may cause the pattern to be mirrored in the target image, therefore ALMA does have a guideline that any extended flux density or long baseline resolution effects should be less than 10% of the core flux for the source to be reliable as the DGC, bandpass or phase calibrator. Of course, the source must be sufficiently strong so that the calibration solutions from it are not significantly S/N limited. The difficulty in finding calibrators at high frequencies while using the longest baseline configuration is that there are few sufficiently bright, perfect pointlike quasars available for DGC or phase referencing, and so calibrators that are slightly extended or resolved must be



**Figure 9.** Distribution of the target scans within the switching cycle time used during the observations. The horizontal axis is the switching cycle time between visits to the phase calibrators. The longer switching cycle times are due to system noise temperature measurement or check source scans being inserted in between phase calibrator scans. From the left, B-08–B-10.

considered. In the case of B2B phase referencing, the systematic phase error due to the calibrator’s structure will also be scaled up by multiplying by  $R$  (although the angular resolution will also be a factor of  $R$  worse, such that there is a lower likelihood of resolving the calibrators) and so we reconducted our reduction to examine any negative effect.

Figure 10 shows synthesized images of J0504-1512 at  $\nu_{\text{LF}}$  (left panels), and J0522-3627 at  $\nu_{\text{LF}}$  and  $\nu_{\text{HF}}$  (middle and right panels, respectively). These show that calibrator sources have extended morphology. In order to investigate how the calibrator structure affects the target image quality, we recreated the target images with B2B phase referencing alone after the structure models of J0504-1512 and J0522-3627 generated from the CLEAN components were provided to the “MODEL” column of the MSs to regenerate the phase and amplitude calibration solutions as described in Section 3.

The top panels of Figure 11 show the recreated continuum images with B2B phase referencing by adopting the structure models of the phase calibrator and DGC source. The difference from the original B2B phase referencing images (assuming calibrators as point sources) as shown in the left panels of Figures 5 and 6 can be hardly recognized. The entire imaged regions are consistent within  $5\sigma$  (image rms noise) in Bands 8–10 as shown in the bottom panels of Figure 11, which depicts the per-pixel differences normalized by the image rms noise of each original target image (Figures 5 and 6). Thus the effect of calibrators’ structure is well within the tolerance of the offered ALMA amplitude accuracy of 10% in Band 8 and 20% in Bands 9 and 10 (Privon et al. 2022) for the R Lep images with dynamic ranges of 255, 98, and 27 in Bands 8–10, respectively. We note that if a high dynamic range is required to image relatively faint structures in a target source, that is a dynamic range down to 3 to orders of magnitude lower than the peak, then the non-pointlike structure of the calibrators may produce image distortions in the outskirts of the brightness distribution. Here for R Lep we consider the differences insignificant.

### 5.3. Image Quality of Check Sources as a Function of Separation Angle

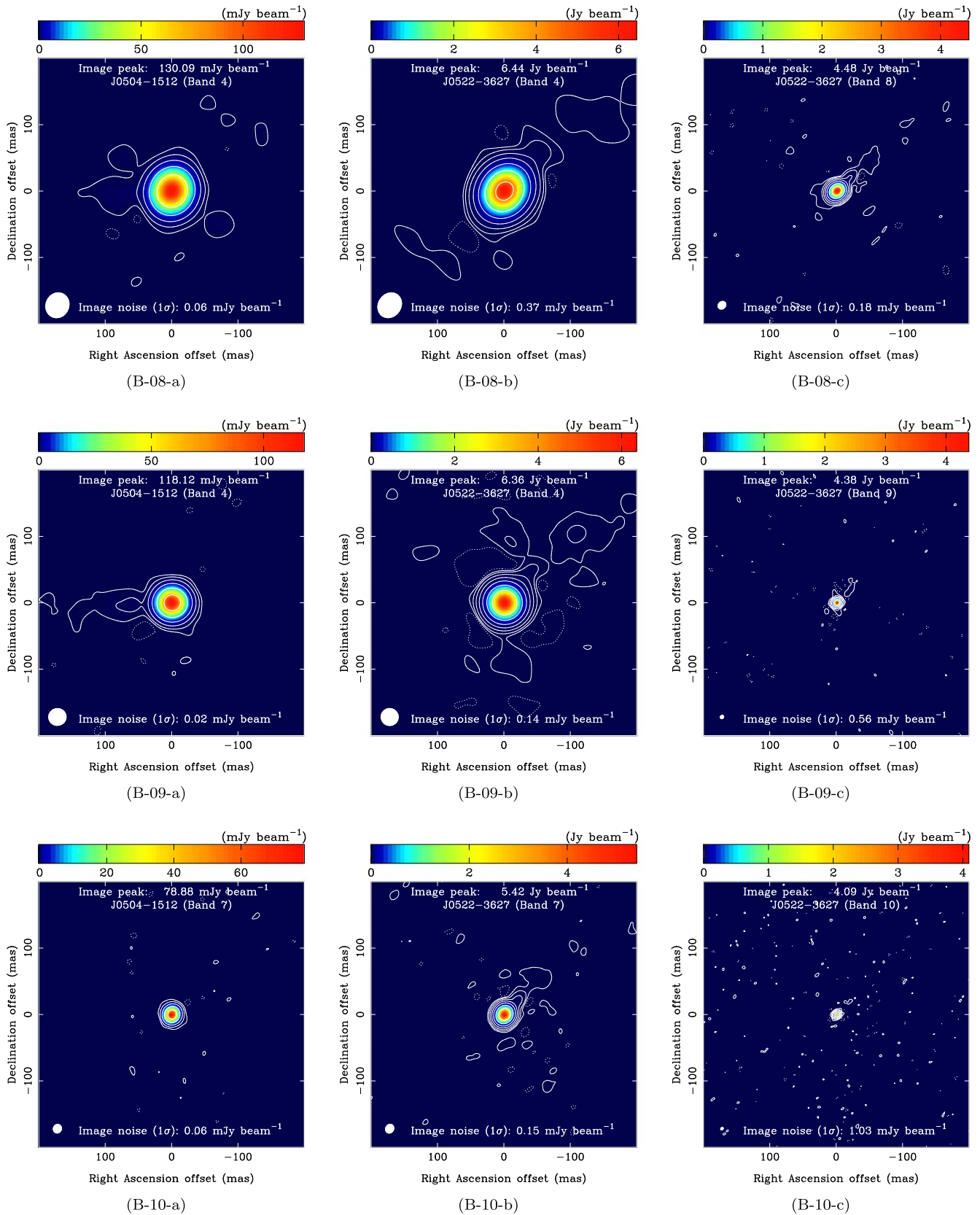
In each experiment, we observed one additional quasar (a check source) to independently assess the data quality. This is a

standard procedure for ALMA HF and long baseline observations. The premise of the check source is to be equally distant from the phase calibrator as the science target is, so that phase solutions from the phase calibrator applied to the check source would be representative of the calibration that the target would receive. However, it is not possible in reality to find such a bright enough quasar in the HF bands, so that the check source is automatically selected in a query to the ALMA online software, which we allowed to select a bright quasar without any restriction on the separation angle to the phase calibrator. In our experiments, J0516-1603, J0438-1251, and J0423-0120 were selected in B-08–B-10, respectively, as listed in Table 2. The separation angle between the check source and phase calibrator (J0504–1512) is  $3^\circ$ ,  $6^\circ.7$ , and  $17^\circ.2$  in B-08–B-10, respectively. Already based upon our previous studies (M20; Maud et al. 2023b), the separation angle for the B-09 and B-10 experiments is too large to be fully representative of the calibration made to R Lep using a phase calibrator at only  $1^\circ.2$  separation.

Figure 12 shows the synthesized images of the check sources of J0516-1603, J0438-1251, and J0423-0120 in Bands 8–10, respectively. The detection in Bands 8 and 9 can be confirmed, Band 8 appearing pointlike indicative of good phase calibration, while that in Band 9 is distorted. In Band 10, there is no detection of the known point source. This illustrates the combined effects of increasing frequency and increasing angular separation on reducing the effectiveness of phase referencing. This reinforces the need to use a phase calibrator at a closer angular separation in general, and moreover highlights the use of B2B phase referencing as the mode to provide a phase calibrator within  $<3^\circ$  in the HF bands. As noted, check sources should be found equidistant from the phase calibrator as the target source is, although given the low likelihood of finding a phase calibrator in the first instance, the possibility of finding another quasar at the HF bands is very difficult. The images of check sources that are further away from the phase calibrator than the target must be interpreted with caution.

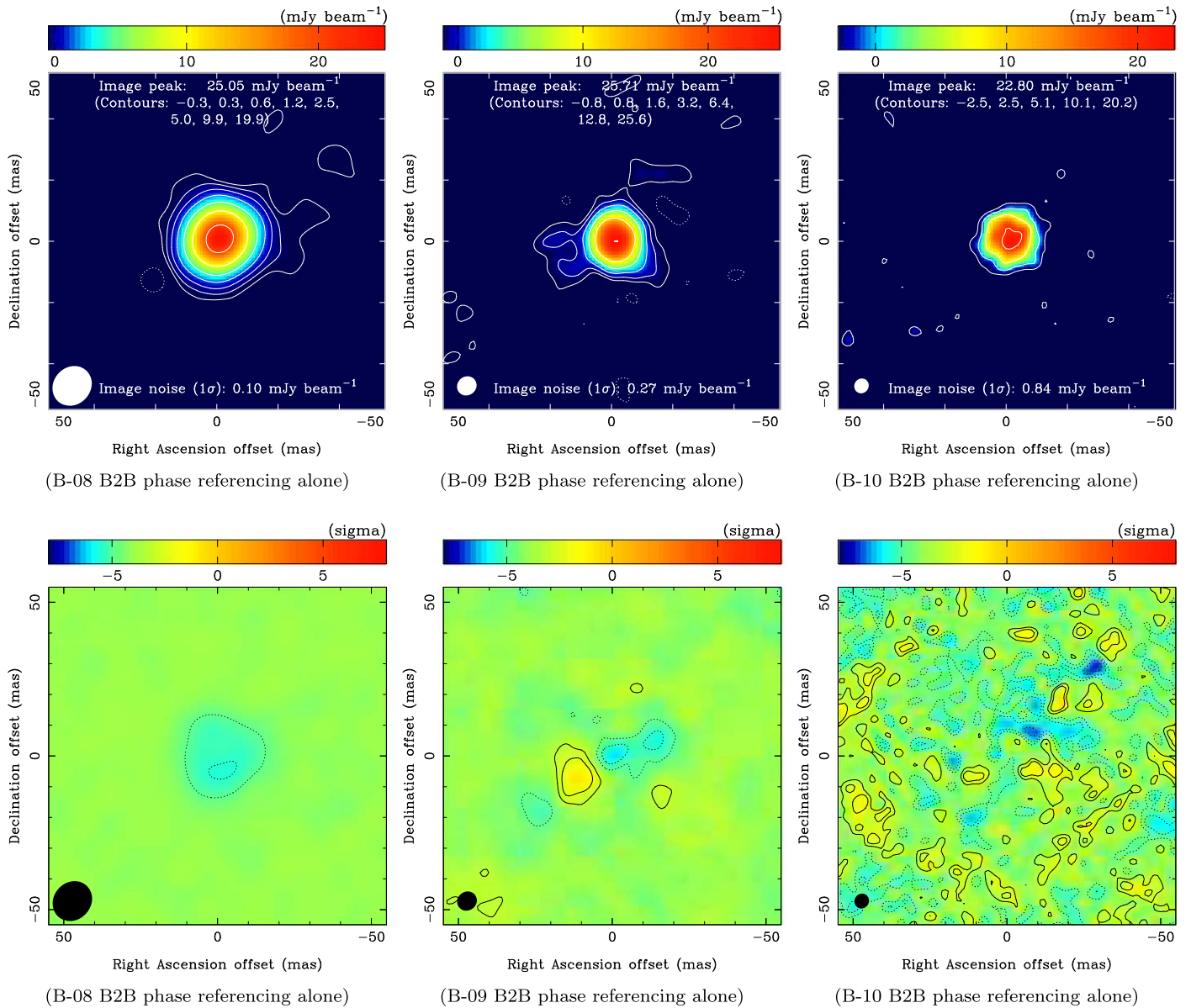
### 5.4. User’s Perspective for HF-LB Observations in ALMA Cycle 9

From the user perspective, there is no required special treatment for HF long baseline observations as are offered from



**Figure 10.** Synthesized images of the calibrators observed in the HF-LBC-2021 experiment. The top, middle, and bottom rows show the images at B-08–B-10, respectively. Left, middle, and right panels show the images of (a) J0504-1512 (phase calibrator) in the LF band, (b) J0522-3627 (DGC source) in the LF band, and (c) J0522-3627 (DGC source) in the HF band, respectively. The solid line contours start from  $3\sigma$  level, increasing by a factor of a power of 4. The dashed line contours start from  $-3\sigma$  level, increased by a factor of a power of 4. The image peak and rms noise are given at the top and bottom of each panel, respectively. The ellipse in the lower left represents the synthesized beam of the image.





**Figure 11.** Top: R Lep continuum images calibrated with B2B phase referencing alone, adopting the calibrator morphology model as shown in Figure 10. From the left, B-08–B-10. The solid line contours start from the  $3\sigma$  level of R Lep continuum image without modeling the calibrator morphology, increased by a factor of a power of 2, and the dashed line contour denotes the  $-3\sigma$  level. The contour levels are shown on the upper side of each panel. Bottom: differential images of the R Lep continuum calibrated with B2B phase referencing alone between the calibrators’ point-source assumption and morphology modeling, normalized by the image rms noise. From the left, B-08–B-10. The color scale ranges between  $-8\sigma$  and  $8\sigma$ . The contours are  $-4\sigma$ ,  $-2\sigma$ , and  $-\sigma$  (dashed lines), and  $\sigma$ ,  $2\sigma$ , and  $4\sigma$  (solid lines).

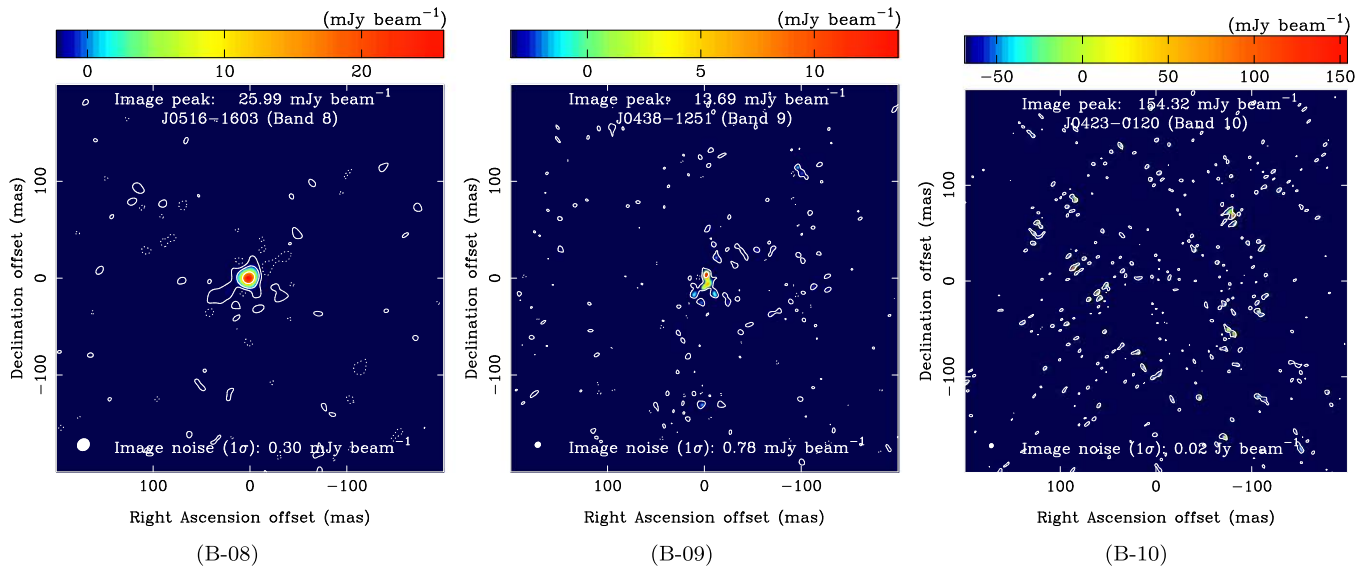
2022 October in Cycle 9. The user can set up their proposals in the ALMA Observing Tool (OT) in the same fashion as any other frequency band or configuration project. In particular, based upon the aforementioned HF-LBCs, the work detailed in Maud et al. (2023b) and in this paper, the OT checks the ALMA calibrator source catalog for suitable bright and close point-source phase calibrators during the project validation for Bands 8–10 observations with long baseline configurations. Information about the stringent angular separation limits for the phase calibrator to target separation is detailed in the ALMA Proposer’s Guide (Privon et al. 2022).

Due to the difficulty in finding bright enough phase calibrators at high frequencies, it is a recommended practice for users to include wider bandwidth spectral windows in order to raise the gain solution S/N if such a setup is feasible for their given science proposal. If the OT search cannot find a suitable

phase calibrator, it automatically switches to a B2B phase referencing calibrator and searches at a predetermined lower frequency band (A20). The observation feasibility for approved proposals is ultimately confirmed by the ALMA observatory prior to the observation taking place. During any B2B phase referencing mode observations the DGC source is added into the observing run by the ALMA online software, as is done for standard calibrators such as the bandpass calibrator in normal observations.

## 6. Summary

The HF-LBC-2021 experiments to image the carbon-rich star R Lep demonstrated that the highest angular resolution ALMA observation at the largest configuration and highest frequencies can produce images with an image coherence of



**Figure 12.** Check source images of J0516-1603 ( $3^\circ$  from the phase calibrator) in Band 8 (left), J0438-1251 ( $6^\circ7$ ) in Band 9 (middle), and J0423-0120 ( $17^\circ2$ ) in Band 10 (right). The horizontal and vertical axes represent relative R.A. and decl. in mas, respectively. The synthesized beam is drawn at the bottom left corner. Contours start from the  $3\sigma$  level, increasing by a factor of a power of 4. The dashed line contours start from the  $-3\sigma$  level, increased by a factor of a power of 4. The image peak value and rms noise are listed at the top and bottom of each panel, respectively. It is clear that for larger separation angles from the phase calibrator that the check sources cannot be correctly calibrated.

$>70\%$ . The use of B2B phase referencing, especially in Bands 9 and 10, will normally be needed to find a suitable phase calibrator close enough to the target. In order to reach the image coherence of  $\geq 70\%$ , observations must be made under stable atmospheric conditions as judged from the 120 s Go/NoGo check before an intended observation. A reasonable Go/NoGo criterion is that the 120 s phase rms is  $\leq 63^\circ$  for the longest quartile of the baseline lengths, although a value of  $\leq 45^\circ$  is preferred and will result in improved image coherence. This Go/NoGo criterion applies to ALMA HF long baseline observations from Cycle 9 (2022 October). Fast switching between the phase calibrator and the target source during phase referencing also allows for good phase calibration, correcting the majority of the fast-changing tropospheric phase errors above each antenna.

The images of the ALMA online software selected check sources highlighted how increasing distance from the phase calibrator can result in poor calibration. The smaller the separation angle from the phase calibrator is, the better the image quality is. The image quality of the check sources demonstrates that the phase calibration can work effectively using nearby phase calibrators of  $<3^\circ$  from the target. In reality, the phase calibrator should ideally be located within  $\sim 1^\circ$  of the science target in the highest frequency bands (Bands 9 and 10) with the longest baselines of 16 km (Maud et al. 2023b). The image coherence of R Lep in all our experiments is  $>70\%$ , achievable by following the Go/NoGo criteria and using a close phase calibrator. B2B phase referencing is likely the only method to find sufficiently close phase calibrators as to achieve high phase calibration performance.

The submillimeter photosphere and HCN maser CSE ring of R Lep were imaged with a 5 mas synthesized beam in Band 10. Self-cal did improve the image quality for the bright and compact HCN maser channel at the LSRK velocity of  $9.4 \text{ km s}^{-1}$  which was then transferred to the other HCN maser channels and to the Band 10 continuum data. However, self-cal is not always applicable to all science targets, especially with

low S/N. Here for R Lep, Band 9 and 10 continuum self-cal resulted in the loss of the longest baselines and demonstrates the limit of useful *weak* source self-cal.

Our work has clarified the optimal observation parameters for HF long baseline observations with B2B phase referencing as detailed in our previous studies (M20; M22; Maud et al. 2023b). The knowledge from this work and the validation experiments constituting the HF-LBCs (A20; Asaki et al. 2020b; M20; M22; Maud et al. 2023b) have been used to enable HF long baseline observations for the scientific community, and the practical lessons learned will also be used to guide future ALMA users' observations at the high frequencies using B2B phase referencing with more compact array configurations.

### Acknowledgments










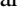



For this research, we made use of the following ALMA data: ADS/JAO.ALMA#2011.0.00009.E, ADS/JAO.ALMA#2011.0.00001.CAL. ALMA is a partnership of ESO (representing its member states), NSF (USA), NINS (Japan), together with the NRC (Canada), NSC and ASIAA (Taiwan), and KASI (Republic of Korea), in cooperation with the Republic of Chile. The Joint ALMA Observatory is operated by the ESO, AUI/NRAO, and NAOJ. The National Radio Astronomy Observatory is a facility of the National Science Foundation operated under cooperative agreement by Associated Universities, Inc. With this paper being published 10 years since ALMA's first observations, we are now illustrating the successful use of Band 10, at the highest frequency and with the longest baselines possible to achieve the highest angular resolution that ALMA can reach. We acknowledge the efforts of many staff, past and present, who have worked on high frequency and/or long baseline and/or B2B and DGC over those last 10 years: Denis A. Barkats, Loreto Barcos-Muñoz, Craige Bevil, Andy Biggs, Crystal Brogan, John M. Carpenter, Arancha Castro-Carrizo, Stuartt Corder, Juan Cortes, Paulo Cortes, Richard Hills, Todd Hunter, Violette Impellizzeri, Katharine Johnston,

Seiji Kamenno, Ryohei Kawabe, Tim Van Kempen, Cristian Lopez, Robert Lucas, Sergio Martin, Satoki Matshushita, Jennifer Donovan Meyer, Anna Miotello, Koh-Ichiro Morita, José Luis Ortiz, Alison Peck, Neil M. Phillips, Vincent Pietu, Adele Plunkett, Alejandro Saez, Tsuyoshi Sawada, Kimberly Scott, Dick Sramek, Ignacio Toledo, Takafumi Tsukui, Baltasar Vila Vilaró, Eric Villard, Catherine Vlahakis, Nick Whyborn, Christine Wilson, although we apologize as the list is not exhaustive, given many staff who have worked behind the scenes, on operations, the hardware and software sub-systems and who work diligently without mention in previous documents or reports. The authors thank an anonymous referee for careful reviews and providing valuable suggestions that greatly improved this paper. K.T.W. acknowledges support from the European Research Council (ERC) under the European Unions Horizon 2020 research and innovation program (grant agreement No. 883867, project EXWINGS).

*Facility:* ALMA (12 m array).

*Software:* CASA (Bean et al. 2022).

### ORCID iDs

Yoshiharu Asaki  <https://orcid.org/0000-0002-0976-4010>  
 Luke T. Maud  <https://orcid.org/0000-0002-7675-3565>  
 Harold Francke  <https://orcid.org/0000-0001-8123-0032>  
 Hiroshi Nagai  <https://orcid.org/0000-0003-0292-3645>  
 Dirk Petry  <https://orcid.org/0000-0002-8704-7690>  
 Edward B. Fomalont  <https://orcid.org/0000-0002-9036-2747>  
 Elizabeth Humphreys  <https://orcid.org/0000-0001-9549-6421>  
 Anita M. S. Richards  <https://orcid.org/0000-0002-3880-2450>  
 Ka Tat Wong  <https://orcid.org/0000-0002-4579-6546>  
 William Dent  <https://orcid.org/0000-0002-2490-1079>  
 Akihiko Hirota  <https://orcid.org/0000-0002-0465-5421>  
 Satoko Takahashi  <https://orcid.org/0000-0002-7287-4343>  
 Antonio S. Hales  <https://orcid.org/0000-0001-5073-2849>

### References

- ALMA Partnership, Brogan, C. L., Pérez, L. M., et al. 2015a, *ApJL*, **808**, L3  
 ALMA Partnership, Fomalont, E. B., Vlahakis, C., et al. 2015b, *ApJL*, **808**, L1  
 ALMA Partnership, Hunter, T. R., Kneissl, R., et al. 2015c, *ApJL*, **808**, L2  
 ALMA Partnership, Vlahakis, C., Hunter, T. R., et al. 2015d, *ApJL*, **808**, L4  
 Andriantsaralaza, M., Ramstedt, S., Vlemmings, W. H. T., & De Beck, E. 2022, *A&A*, **667**, A74  
 Asaki, Y., Matsushita, S., Fomalont, E. B., et al. 2016, *Proc. SPIE*, **9906**, 99065U  
 Asaki, Y., Maud, L. T., Fomalont, E. B., et al. 2020a, *ApJS*, **247**, 23  
 Asaki, Y., Maud, L. T., Fomalont, E. B., et al. 2020b, *AJ*, **160**, 59  
 Asaki, Y., Shibata, K. M., Kawabe, R., et al. 1998, *RaSc*, **33**, 1297  
 Assaf, K. A. 2018, *ApJ*, **869**, 80  
 Barber, R. J., Strange, J. K., Hill, C., et al. 2014, *MNRAS*, **437**, 1828  
 Bean, B., Bhatnagar, S., (CASA Team), et al. 2022, *PASP*, **134**, 114501  
 Biegging, J. H. 2001, *ApJL*, **549**, L125  
 Brogan, C. L., Hunter, T. R., & Fomalont, E. B. 2018, arXiv:1805.05266  
 Brogière, D., Lucas, R., Pardo, J., & Roche, J. C. 2011, in ASP Conf. Ser. 442, *Astronomical Data Analysis Software and Systems XX*, ed. I. N. Evans et al. (San Francisco, CA: ASP), 277  
 Carilli, C. L., & Holdaway, M. A. 1999, *RaSc*, **34**, 817  
 Cortes, P. C., Remijan, A., Hales, A., et al. 2022, ALMA Cycle9 Technical Handbook v1.0, Zenodo, doi:10.5281/zenodo.7764458  
 Cotton, W. D., Mennesson, B., Diamond, P. J., et al. 2004, *A&A*, **414**, 275  
 Dodson, R., & Rioja, M. J. 2009, arXiv:0910.1159  
 Emerson, D. T. 2005, ALMA Memo No. 537, [https://science.nrao.edu/facilities/alma/aboutALMA/Technology/ALMA\\_Memo\\_Series/alma537/abs537](https://science.nrao.edu/facilities/alma/aboutALMA/Technology/ALMA_Memo_Series/alma537/abs537)  
 Farren, G. S., Partridge, B., Kneissl, R., et al. 2021, *ApJS*, **256**, 19  
 Fomalont, E., van Kempen, T., Kneissl, R., et al. 2014, *Msngr*, **155**, 19  
 Guilloteau, S., Omont, A., & Lucas, R. 1987, *A&A*, **176**, L24  
 Hocker, L. O., & Javan, A. 1967, *PhLA*, **25**, 489  
 Hofmann, K. H., Eberhardt, M., Driebe, T., et al. 2005, in 13th Cambridge Workshop on Cool Stars, Stellar Systems and the Sun, ed. F. Favata, G. A. J. Hussain, & B. Battrock, Vol. 560 (Paris: ESA), 651  
 Höfner, S., & Olofsson, H. 2018, *A&ARv*, **26**, 1  
 Hunter, T. R., Lucas, R., Brogière, D., et al. 2016, *Proc. SPIE*, **9914**, 99142L  
 Hunter, T. R., Petry, D., Barkats, D., et al., 2023 analysisUtils v2.90, Zenodo, doi:10.5281/zenodo.8408419  
 Jeste, M., Gong, Y., Wong, K. T., et al. 2022, *A&A*, **666**, A69  
 Leon, S., Cortes, P. C., Guérard, M., et al. 2016, *A&A*, **586**, A70  
 Lucas, R., & Cernicharo, J. 1989, *A&A*, **218**, L20  
 Matsushita, S., Asaki, Y., Fomalont, E. B., et al. 2017, *PASP*, **129**, 035004  
 Matthews, L. D., Reid, M. J., & Menten, K. M. 2015, *ApJ*, **808**, 36  
 Matthews, L. D., Reid, M. J., Menten, K. M., & Akiyama, K. 2018, *AJ*, **156**, 15  
 Maud, L. T., Asaki, Y., Dent, W. R. F., et al. 2022, *ApJS*, **259**, 10  
 Maud, L. T., Asaki, Y., Fomalont, E. B., et al. 2020, *ApJS*, **250**, 18  
 Maud, L. T., Asaki, Y., Nagai, H., et al. 2023b, *ApJS*, **267**, 24  
 Maud, L. T., Pérez-Sánchez, A. F., Asaki, Y., et al. 2023a, arXiv:2304.08318  
 Maud, L. T., Tilanus, R. P. J., van Kempen, T. A., et al. 2017, *A&A*, **605**, A121  
 Menten, K. M., Wyrowski, F., Keller, D., & Kamiński, T. 2018, *A&A*, **613**, A49  
 Nikolic, B., Bolton, R. C., Graves, S. F., Hills, R. E., & Richer, J. S. 2013, *A&A*, **552**, A104  
 Pardo, J. R., De Breuck, C., Muders, D., et al. 2022, *A&A*, **664**, A153  
 Pearson, T. J., & Readhead, A. C. S. 1984, *ARA&A*, **22**, 97  
 Pérez, L. M., Lamb, J. W., Woody, D. P., et al. 2010, *ApJ*, **724**, 493  
 Petry, D., Vila-Vilaro, B., Villard, E., Komugi, S., & Schnee, S. 2014, *Proc. SPIE*, **9152**, 91520J  
 Planesas, P., Alcolea, J., & Bachiller, R. 2016, *A&A*, **586**, A69  
 Privon, G., Nagai, H., Rebolledo, D., & Díaz Trigo, M. 2022, ALMA Cycle 9 Proposer's Guide v1.4, Zenodo, doi:10.5281/zenodo.7662388  
 Ramstedt, S., Vlemmings, W. H. T., Doan, L., et al. 2020, *A&A*, **640**, A133  
 Reid, M. J., & Menten, K. M. 1997, *ApJ*, **476**, 327  
 Richards, A. M. S., Impellizzeri, C. M. V., Humphreys, E. M., et al. 2014, *A&A*, **572**, L9  
 Richards, A. M. S., Moravec, E., Etoka, S., et al. 2022, arXiv:2207.05591  
 Schilke, P., Mehringer, D. M., & Menten, K. M. 2000, *ApJL*, **528**, L37  
 Schilke, P., & Menten, K. M. 2003, *ApJ*, **583**, 446  
 Shillue, B., Grammer, W., Jacques, C., et al. 2012, *Proc. SPIE*, **8452**, 845216  
 Smith, C. L., Zijlstra, A. A., & Fuller, G. A. 2014, *MNRAS*, **440**, 172  
 Thompson, A. R., Moran, J. M., & Swenson, G. W., Jr. 2017, *Interferometry and Synthesis in Radio Astronomy* (3rd ed.; Cham: Springer)  
 Vallenari, A., Brown, A. G. A., (Gaia Collaboration), et al. 2023, *A&A*, **674**, A1  
 van Kempen, T., Kneissl, R., Marcelino, N., et al. 2014, ALMA Memo No. 599, [https://science.nrao.edu/facilities/alma/aboutALMA/Technology/ALMA\\_Memo\\_Series/alma599/memo599.pdf/view](https://science.nrao.edu/facilities/alma/aboutALMA/Technology/ALMA_Memo_Series/alma599/memo599.pdf/view)  
 Vlemmings, W. H. T., Khouri, T., & Olofsson, H. 2019, *A&A*, **626**, A81  
 Vlemmings, W. H. T., Ramstedt, S., O'Gorman, E., et al. 2015, *A&A*, **577**, L4  
 Watson, C. L., Henden, A. A., & Price, A. 2006, *SASS*, **25**, 47  
 Wong, K. T. 2019, ALMA2019: Science Results and Cross-Facility Synergies (Garching: ESO), **55**, <http://www.eso.org/sci/meetings/2019/ALMA2019Cagliari.html>  
 Wong, K. T., Kamiński, T., Menten, K. M., & Wyrowski, F. 2016, *A&A*, **590**, A127